A three-dimensional mechanistic study of the drivers of classical twin nucleation and variant selection in Mg alloys : a mesoscale modelling and experimental study

Chaitanya Paramatmuni *[a], Yi Guo [a], Philip J. Withers [b], Fionn P.E. Dunne [a]

a. Department of Materials, Imperial College London, London SW7 2AZ, United Kingdom
b. Henry Royce Institute, Department of Materials, University of Manchester, Manchester M13 9PL, United Kingdom

Abstract

This work presents a detailed investigation of twin inception to identify site of twinning, variant type selected, and the strain to nucleate it within a full 3D reconstructed microstructure obtained using 3D-EBSD. Microstructurally-faithful 3D crystal plasticity analysis provides quantitative insight to show that stored energy density is a key factor (rather than stress or other criteria) which identifies the experimentally observed twin nucleation site (which supersedes twin inception), and the strain necessary to drive nucleation. 3D (as opposed to 2D surface) analysis has been shown to be essential. The *critical* energy density for twin nucleation was found to be ~0.015 Jm^{-2} in Mg alloy AZ31. Further, at the predicted nucleation site, the experimentally observed twin variant is shown to be driven by the local twin resolved shear stress.

Keywords

Crystal plasticity finite element method; deformation twinning; stored energy density; twin nucleation site; twin resolved shear stress.

*Corresponding author
Email address: chaitanyaparamatmuni@gmail.com

1. Introduction

The current study aims to achieve a mechanistic understanding of the deformation twin nucleation sites and associated variant selection within magnesium (Mg) alloy AZ31, a representative candidate of hexagonal close-packed (HCP) materials. The novelty of this work lies in the detailed investigation of the twin nucleation sites and variant types in three dimensions (3D) within a deformed, reconstructed microstructure obtained using block face serial section 3D-EBSD (Echlin et al. (2020)). The consideration of the 3D microstructure allows a detailed layer-by-layer experimental and numerical analysis of the drivers of twin nucleation. It is important to understand twin nucleation as it may allow texture modification to inhibit twinning, which otherwise results in a complex deformation response (Easton et al. (2008)) leading to poor room-temperature formability (Kumar et al. (2017)) and also causes initiation of material failure (Al-Samman and Gottstein (2008), Yang et al. (2008), Hazeli et al. (2015)).

Although the formation of twinning is being actively explored, twin nucleation has not been studied in 3D with thorough experimental comparisons. Twin formation is broadly considered to comprise three stages: nucleation, propagation and growth (Christian and Mahajan (1995)). In heterogeneous twin nucleation, which is supported by much experimental and numerical evidence, the twin nucleus forms either by stress assisted dissociation of dislocations that occur due to plasticity within parent grains at the grain boundaries (Mendelson (1969), Barrett et al. (2012), Jeong et al. (2018)) and/or due to the interaction between the dislocations and the parent grain boundaries (e.g. Wang et al. (2014)). The type of mechanism leading to the formation of twin nuclei may be related to the parent grain orientation. While in less favourable grains (global Schmid factor of ~0.3) the formation of twin nuclei may result from the dissociation of dislocations (accumulated as a result of plasticity within parent grain) and/or interaction between dislocations and parent grain boundaries, the formation of twin nuclei in the most

favourable grains may not require the presence of dislocations. Several experimental and modelling approaches have been developed across length-scales to understand the twin nucleation process (Bell and Cahn (1953), Price (1961), Capolungo et al. (2009), Wang et al. (2009a), Wang et al. (2009b), Beyerlein and Tomé (2010), Wang et al. (2010b), Wang et al. (2010a), Beyerlein et al. (2011), Wang et al. (2013), Barnett et al. (2014), Prasad et al. (2014), Abdolvand et al. (2020)). However, before a stable twin nucleus forms, there exists an incubation/inception period, where the dislocations in the parent grain develop and accumulate at the grain boundaries. The interaction between these dislocations and/or between dislocations and grain boundaries increases local stresses, thereby increasing the energy that is stored in the material in the form of local dislocation structures.

The evolution of this local stored energy during twin inception has been utilized in several numerical studies to account for twin nucleation, wherein the dissociation of accumulated $\langle a \rangle$ or $\langle c + a \rangle$ dislocations occur only after the local energy reaches a critical value (Capolungo and Beyerlein (2008), Ghazisaeidi and Curtin (2013), Cheng and Ghosh (2015)). In other non-energy based approaches, either an 'imperfection' that drives nucleation (Qiao et al. (2016)) or the twin nucleus itself is introduced within the (single/bi-crystal) computational domain (Liu et al. (2018)). In other approaches twinning is treated as pseudo-slip and the twin volume fraction is used to describe deformation by twinning (Tomé et al. (1991), Abdolvand et al. (2011), Wu et al. (2015), Paramatmuni and Kanjarla (2019)). However, these approaches need like-for-like comparison with the experimental data in 3D. In summary, twin inception precedes the nucleation stage and tracking the evolution of local stored energy at the twin inception sites allows precise identification of twin nucleation locations, where local stored energy reaches some critical value.

In this context, Paramatmuni et al. (2020) showed that the total stored energy density is a promising candidate for locating the twin nucleation sites (twin inception site after total stored

energy reaches a critical value). It was shown that the total stored energy density locates the twin nucleation site within unfavourably oriented parent grains and the shear stored energy density drives variant selection (Paramatmuni et al. (2020)). Although this and other numerical approaches attempt to provide a mechanistic understanding of twin nucleation, there are two limitations. These studies are typically based on experimental evidence obtained on 2D (free) surfaces and use pseudo 3D domains, which lack the subsurface information, to simulate twin formation. In addition, it is known that twins are 3D defects (Liu et al. (2019)) that may nucleate in the subsurface and propagate to the free surface of the sample. Thus a detailed 3D microstructural information is essential to locate twins in parent grains and to study their formation.

In the present work, as a first step, these limitations are overcome by performing 3D-EBSD to obtain the 3D microstructure of a deformed small-scale pillar fabricated from the bulk Mg alloy AZ31. The aim of the present work is to investigate the precursors that drive twin nucleation (potential twin inception sites that reach a critical value of stored energy) in the parent grains as distinct from modelling the progressive formation of twin nuclei. Within this full 3D microstructure, a grain and a twin of interest are identified to locate the potential twin nucleation site and to identify the active variant type. As the main aim of this paper is to provide a mechanistic view of the drivers of twin nucleation, which requires analyses of the parent grain and corresponding twin in 3D, only a single parent-twin pair is investigated in great detail. The current 3D study in conjunction with the previous study of twin nucleation (Paramatmuni et al. (2020)), provides broader statistical evidence for the proposed drivers of twin nucleation. The uniaxial deformation of the undeformed 3D microstructure is then simulated within a crystal plasticity finite element framework by adopting realistic boundary conditions. This allows systematic study of the 3D distribution of deformation variables to understand the mechanistic drivers of twin nucleation and variant selection. Here the main focus is on locating

twin nucleation sites that occur only due to dissociation of accumulated dislocations at parent grain boundaries when the local stored energy reaches a critical value, rather than that caused by the interaction between the dislocations and the parent grain boundaries (e.g. Wang et al. (2014)). As a result we do not need to consider an explicit definition of the grain boundaries within the computational framework.

2. Methods

This section details material characterisation, small-scale pillar fabrication and the procedure followed to generate the deformed 3D microstructure.

2.1 Material preparation and characterization

Mg alloy AZ31 was received as warm-rolled plate with dimensions, composition and strong basal texture, as detailed in (Paramatmuni and Dunne (2020)). The as-received material with an average grain size of 11 μm, was annealed at 525 °C for 24 hours to obtain a suitable grain size for 3D-EBSD. In order to avoid excessive oxidation at the annealing temperatures, the sample was maintained in an argon atmosphere before furnace cooling post heat treatment. After annealing, it was mechanically polished to 4000 grit silicon carbide paper followed by fine polishing using 50 nm colloidal silica suspension for about 30 minutes. The sample was then Ar ion polished with a PECS-II system under dual beam condition using 4.0 keV beam energy with rotational speed of 4 rpm for about 40 minutes, followed by 20 minutes fine polishing using 2.0 keV and a speed of 2 rpm. The average grain size was measured by performing EBSD in a ZEISS Sigma 300™ SEM equipped with Bruker high resolution EBSD detector with voltage of 20 kV and ~13 mm working distance.

Once the material with appropriate average grain size was obtained, a small pillar of dimensions ~0.5x0.5x0.9 mm^3 and taper angle of ~2° was fabricated by an initial rough laser

cut using Gatan microPREP, and then fine polished using an FEI Helios PFIB (Xe^+) with voltage 30 kV and current 59 nA.

2.2 Uniaxial compression, serial sectioning and EBSD

The small-scale pillar was compressed to 4% strain at a rate of 0.002 s^{-1} in a Deben Microtest 200 N stage. After deformation, an FEI Helios Dual Beam PFIB-SEM equipped with Oxford Instruments NordlysNano EBSD detector was used for block face serial sectioning followed by EBSD of the newly revealed surface (see Burnett et al. (2016) for technical details). Serial sectioning was conducted parallel to the Z-axis (loading direction) on a volume of 350 x 350 x 235 μm^3 with a section thickness of 0.5 µm resulting in 470 (X-Y) slices. Before commencing the 3D-EBSD process, some material on the top surface of the pillar was removed to obtain a clean surface for EBSD. The PFIB was operated at a voltage of 30kV and 59 nA current using a rocking polish of ± 3° leading to a sectioning time of 2-3 minutes per slice. After removing the slice, the surface was characterized by EBSD using a voltage of 20 kV and a working distance of 9.2 mm, 4x4 binning and a step size of 0.5 µm was used to give cubic voxels ($0.5\mu m^3$) for the 3D microstructure reconstruction.

Dream3D (Groeber and Jackson (2014)) was used for reconstruction of the 3D data from the unaligned 2D EBSD slices. The raw EBSD slices were first stacked using an appropriate reference frame taking into account the slice thickness (0.5 µm). The top 28 slices (~14 µm) were omitted from the reconstruction to ensure that only the best quality EBSD slices were included in the analyses. The unaligned 3D data were filtered to identify voxels with poor indexing. These unreliable voxels were removed by introducing two more filters based on misorientation and confidence index of neighbouring voxels, where the data from unreliable voxels were replaced by that of neighbouring reliable ones. The alignment of slices in the Z-direction was achieved by using two filters based on the reliability of data (indexing quality)

and misorientation angle between the sections. The aligning process during data reconstruction, adjusted sections in the XY plane to give the best overlap between them. After the alignment process, the features (parent grains and twins) were segmented based on misorientation angle (tolerance of 2.5°) to obtain grains, twins and unindexed data. Then the grains and twins were segmented further based on their respective feature sizes. Finally, these aligned and segmented data were filtered again to remove/fill poor quality data.

2.3. Computational framework and material properties

The crystal plasticity finite element formulation developed in Dunne et al. (2007), which is implemented in ABAQUS FE solver as a user subroutine (UMAT) that accounts for strain gradients and rate-sensitivity, is employed here to address the development of mechanical field quantities which may ultimately lead to the formation of twin nuclei.

Pointwise deformation comprises shear of the crystal lattice (slip), elastic distortion and rigid body rotation. Thus the total deformation gradient $\mathbf{F}$ can be decomposed into elastic ($\mathbf{F}^{e}$) and plastic deformation gradient tensors ($\mathbf{F}^{p}$) as

$$\mathbf{F} = \mathbf{F}^{e}\mathbf{F}^{p} \tag{1}$$

The crystallographic shear rates from all slip systems result in the plastic velocity gradient

$$\mathbf{L}^{p} = \sum_{\alpha} \dot{\gamma}^{\alpha}\mathbf{s}^{\alpha} \otimes \mathbf{n}^{\alpha} \tag{2}$$

where $\mathbf{n}^{\alpha}$ and $\mathbf{s}^{\alpha}$ are the plane normal and direction of slip system α respectively. The slip rates recognising both forward and backward thermally activated dislocation escape are given by

$$\dot{\gamma}^{\alpha} = \rho_{m} b^{\alpha 2} \nu_{D} \exp\left(-\frac{\Delta F}{kT}\right) \sinh\left(\frac{(\tau^{\alpha} - \tau_{c}^{\alpha})\Delta V^{\alpha}}{kT}\right) \tag{3}$$

in which ρ_m is the mobile dislocation density, b^α the magnitude of the Burgers vector, ν_D the Debye frequency, k the Boltzmann constant, T the temperature, and τ^α and τ_c^α are the resolved shear stress (RSS) and the corresponding critical resolved shear stress (CRSS) for the slip system α. The strain rate sensitivity is determined by the activation energy ΔF and a corresponding activation volume ΔV^α for the slip system α. The evolution of the CRSSs is defined using the isotropic Taylor's equation used in Paramatmuni and Dunne (2020) for hardening due to the evolution of statistically stored and geometrically necessary dislocations,

$$\tau_c^\alpha = \tau_o^\alpha + \zeta_h^\alpha G b^\alpha \sqrt{\rho_{ssd} + \sum_{\beta=1}^{n} \rho_{gnd}^\beta} \tag{4}$$

where τ_o^α is the initial friction stress of the slip system α, G is the shear modulus of the material and ζ_h^α is the hardening coefficient for a given slip system α, which accounts for different hardening rates of the slip systems.

The evolution of statistically stored dislocations (SSDs) is given as

$$\rho_{ssd} = \Gamma \int_0^t \dot{\epsilon}_{eff}^p \, dt \tag{5}$$

where Γ is an isotropic hardening coefficient and $\dot{\epsilon}_{eff}^p$ is the effective plastic strain rate defined as $\sqrt{\frac{2}{3}\left(\dot{\bar{\epsilon}} : \dot{\bar{\epsilon}}\right)}$, and $\dot{\bar{\epsilon}}$ is the plastic strain rate tensor.

The distribution of geometrically necessary dislocation (GND) density is calculated from the strain gradients accommodating lattice curvatures that are represented using the Nye tensor (Nye (1953)), which is determined from the curl of plastic deformation gradient tensor. The Nye tensor is related to the GND density on an individual slip system by

$$\text{curl}\left(\mathbf{F_p}\right) = \sum_{\alpha=1}^{n} \mathbf{\Lambda}^\alpha \rho_{gnd}^\alpha \tag{6}$$

where $\boldsymbol{\Lambda}^{\alpha}$ is the second order tensor that contains the crystallographic information of the slip systems (see (Arsenlis and Parks (1999)) and ρ_{GND}^{α} the GND density on slip system α. Many metals give rise to more active slip systems than the nine independent components of the dislocation density tensor, so that the solution to eq. 6 is non-unique. Thus, the L1 minimization scheme detailed in Paramatmuni and Dunne (2020) is used to obtain the GND density, which is shown to satisfactorily predict the experimental trends (also see Paramatmuni et al. (2020)).

The material properties including elastic constants obtained in Paramatmuni and Dunne (2020) for Mg alloy AZ31 are used in the current study. In summary, 12 slip systems - three basal slip systems $< 11\bar{2}0 > \{0001\}$, three prismatic slip systems $< 11\bar{2}0 > \{10\bar{1}0\}$, six pyramidal slip systems $< 11\bar{2}3 > \{\bar{1}\bar{1}22\}$ - are considered. The rate sensitive single crystal properties are summarized in table 1.

Table 1: Single crystal elastic and slip parameters for Mg AZ31 at room temperature (Paramatmuni and Dunne (2020))

Elastic constants							
C_{11}=58.0, C_{12}=25.0, C_{13}=20.8, C_{33}=61.2, C_{44}=16.6 (GPa) (Tromans (2011))							
Slip parameters							
Mode	τ_o^{α}	ΔV^{α} (b^3)	ζ_h^{α}	ΔF (J)	ρ_m (μm^{-2})	V_D (s^{-1})	Γ (μm^{-2})
Basal	12	62.5	0.15	7.5×10^{-20}	1	1.2×10^{13}	750
Prismatic	62.4	62.5	0.4				
Pyramidal II order	108	5	1.0				

In order to investigate the location of twin nucleation sites, the total stored energy density approach presented by Paramatmuni et al. (2020) is used. In addition, Xu et al. (2021), in their crystal plasticity modelling, analytical and experimental study of the effect of microstructure on fracture mechanics, also recently reported a good agreement between the numerical and the experimental stored energy density ahead of a crack tip. This energy density is that stored in the material resulting from dislocation structures formed during plastic deformation. In particular, Zheng et al. (2019) showed that this energy is stored preferentially within GND structures, which attributes a characteristic length scale to this quantity. Thus, the length scale associated with this quantity is that of dislocations within the parent grain that potentially drive twin nucleation. Paramatmuni et al. (2020) showed that this criterion successfully predicts the nucleation sites of twins within unfavourable parent grains as it is a measure of available local defect and energy sources in the microstructure. In the context of twins, it is shown in independent experimental studies that the dissociation of local dislocation structures leads to the formation of twin nuclei (Jeong et al. (2018)). In Paramatmuni et al. (2020), 5% of total energy due to plastic deformation is taken as that stored in dislocation structures with the remaining 95% dissipated as heat. The accumulated total stored energy density G_{SE} at each point in the microstructure is

$$G_{SE} = \int \frac{\zeta |\boldsymbol{\sigma} : d\boldsymbol{\varepsilon}^{p}|}{\sqrt{\rho_{SSD} + \sum_{i=1}^{n} \rho_{GND}^{i}}} \tag{7}$$

in which ζ represents the fraction of plastic energy stored locally, i.e. $\zeta = 0.05$. Zheng et al. (2019) using discrete dislocation plasticity (DDP) modelling recently demonstrated that this assumption of 5% is reasonable such that equation (7) agrees well with the local dislocation configurational energy calculated in their DDP studies.

3. Results

3.1 Reconstructed 3D deformed microstructure, grain and twin of interest

Fig. 1(a) shows the heat treated twin-free microstructure with an average grain size of 55 µm and Fig. 1(b) the small-scale pillar, which may contain ~150 grains, fabricated from a bulk cube (5x5x5 mm^3) of Mg alloy AZ31 such that the pillar is supported by a base. Loading was parallel to the rolling direction, which causes extension twinning dominated yielding of the

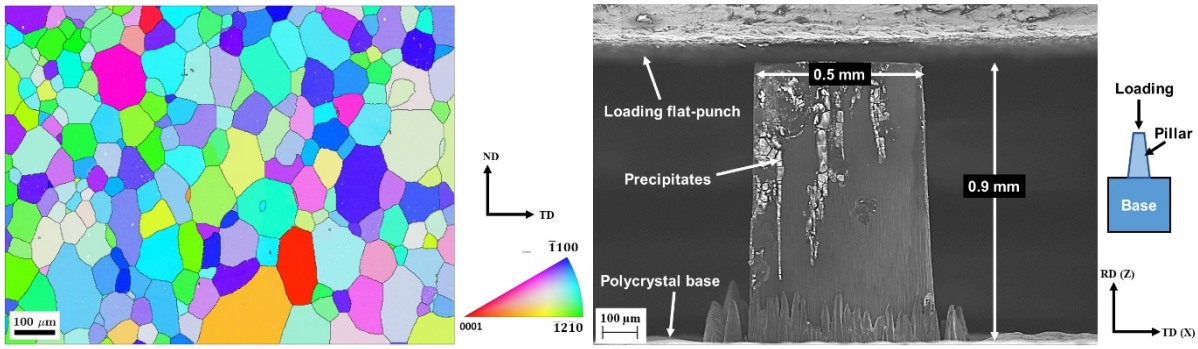

(a) (b)

Figure 1: The undeformed material: (a) IPFZ map of the heat treated sample and (b) SEM micrograph showing the undeformed small-scale pillar of dimensions ~0.5x0.5x0.9 mm^3 fabricated from bulk Mg alloy AZ31, where RD (Z) is the loading direction and TD||X, ND||Y.

pillar. The surface of the pillar in Fig. 1(b) shows precipitates ($Mg_{17}Al_{12}$) that have grown to a considerable size due to heat treatment.

The small scale pillar is deformed at room temperature until 4% strain at the strain rate of 0.002 s^{-1}. Fig. 2 shows the top view and the side views of the deformed pillar. From the top view, the deformation appears to be uniform without any evidence of buckling. This is further confirmed in the side views that show macroscopic uniform deformation with some barrelling, as seen in faces 2 and 4. After uniaxial compression, the pillar is subjected to serial sectioning followed by EBSD of each slice. Fig. 3 shows the sequence of steps followed in obtaining a reconstructed 3D deformed microstructure. The deformed pillar shown in Fig. 3(a) is serial sectioned along

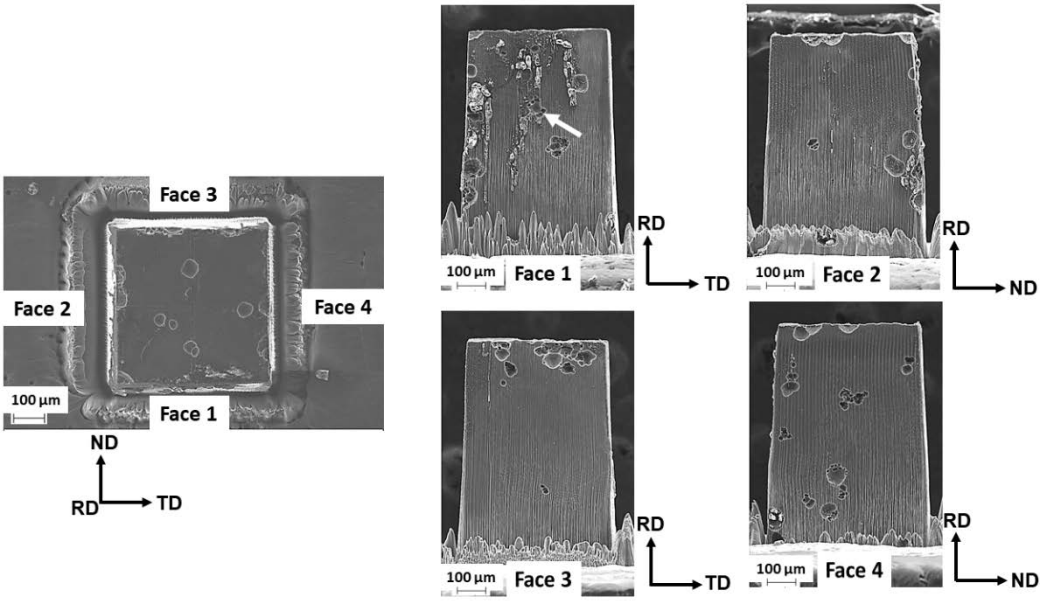

Figure 2: The SEM micrographs of deformed small-scale pillar showing homogeneous deformation without buckling. The white arrow indicates the craters on the surface formed due to detached precipitates.

the loading (Z) direction to obtain 470 EBSD slices, as shown in Fig. 3(b). Fig. 3(c) shows the unaligned stack of EBSD data that is in the form of a cube, where the colour of grains and twins represent their respective feature identification numbers (IDs). After implementing the data reconstruction steps explained in section 2.2, the resulting aligned 3D microstructure is shown in Fig. 3(d). The alignment process translates sections in the XY plane to obtain the best registry

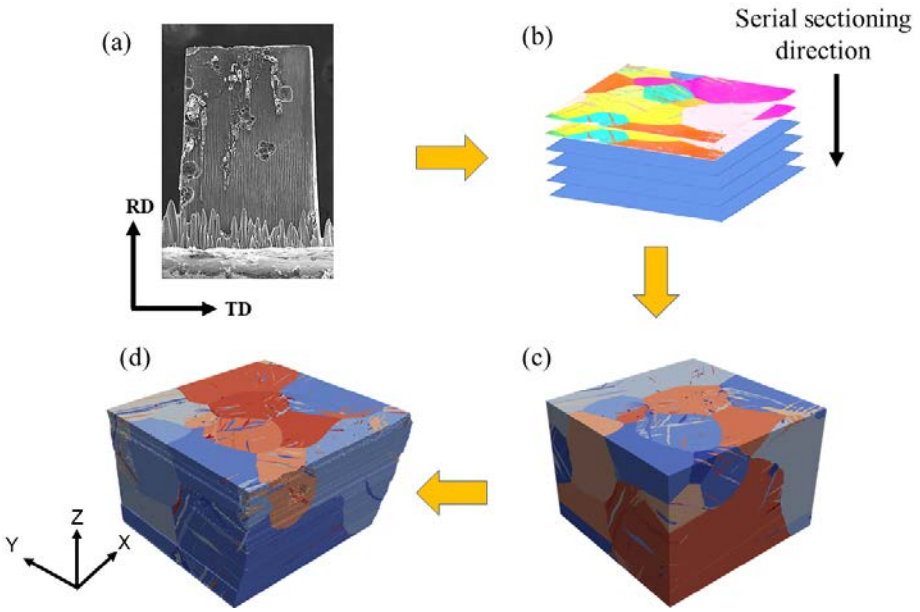

Figure 3: The sequence of steps involved in generating the reconstructed 3D deformed microstructure showing (a) the deformed pillar, (b) a schematic of the serial sections showing the sectioning direction, (c) the stack of unaligned EBSD slices and (d) the final outcome after aligning the EBSD slices and data processing.

between them, which leads to heterogeneities on the outer surface of the reconstructed 3D microstructure.

The reconstructed 3D microstructure consists of 34 grains. In this work, extension twins are classified as non-classical and classical based on the corresponding parent grain orientations and the mechanical fields that drive their nucleation and variant selection. Non-classical twins are those that are active in unfavourably oriented parent grains, where their nucleation is driven mainly by local stored energy (Paramatmuni et al. (2020)) and/or strain gradients (McClelland et al. (2015), Molodov et al. (2016)). In contrast, classical twins are those that nucleate within favourably oriented parent grains, which are considered to be driven by local stress fluctuations (Qiao et al. (2016)). In order to investigate and locate twin nucleation sites, a grain of interest is first identified within the microstructure based on two criteria : (a) favourable orientation for twinning (classical twin), (b) the entirety of the grain should be well within the microstructure with some distance from the free surfaces. Fig. 4(a) shows the selected grain of interest (GOI), where it is embedded within the microstructure, situated well away from the side free surfaces and a few microns away from the top free surface. Note that this grain lies at a considerable distance from the original top (loaded) surface of the sample. As mentioned earlier, some material is removed before serial sectioning to obtain a good surface finish and the first 28 slices are not considered in the reconstruction process. In addition, Fig. 1(b) shows the presence of precipitates on the surface of the small-scale pillar. While the detailed analysis of the reconstructed 3D volume of the microstructure does not show the presence of these precipitates within the grain of interest, it is shown in other studies that the former has a negligible influence on twin nucleation (Robson et al. (2010), Stanford et al. (2012), Wang and Stanford (2015), Wang et al. (2019), Robson and Barnett (2019)). Thus, the precipitates are not considered in subsequent experimental and numerical analyses.

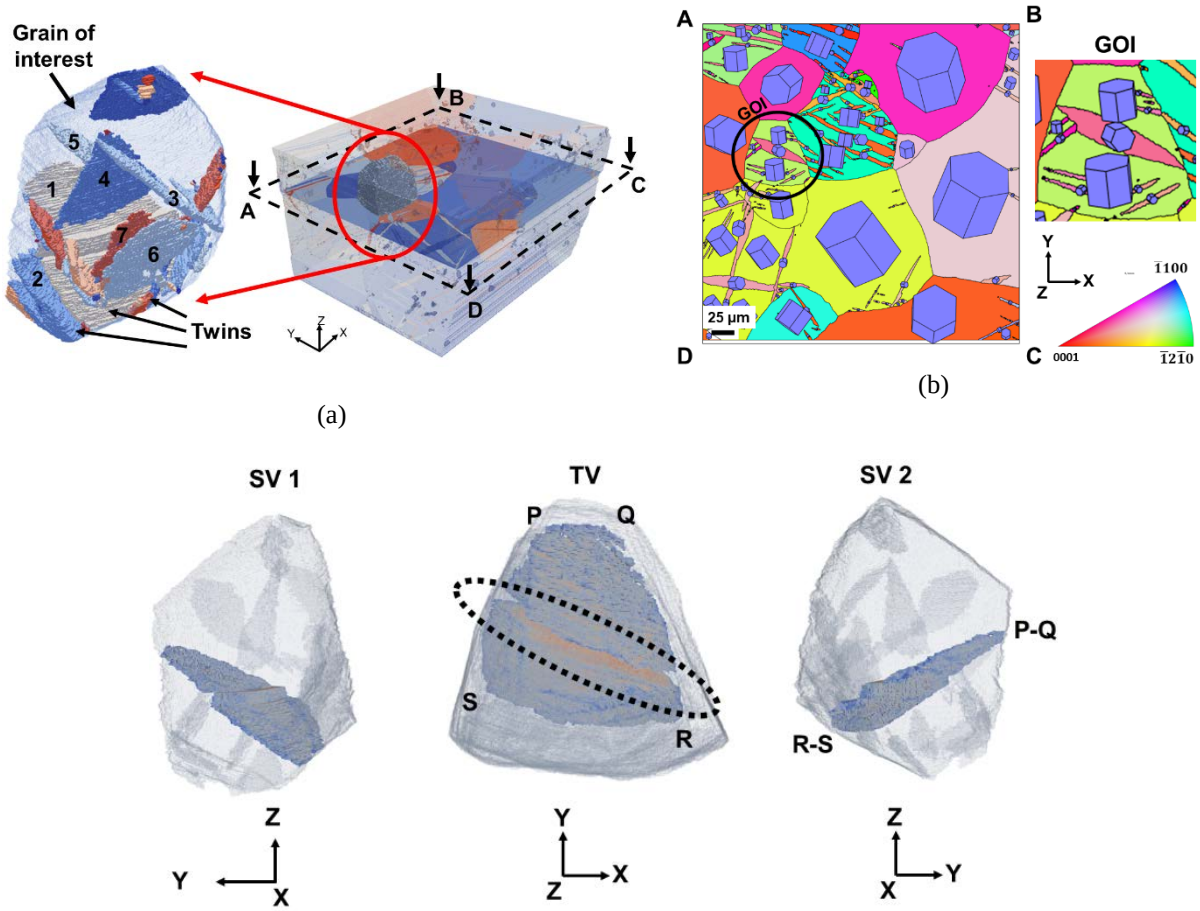

Figure 4: The deformed microstructure (compressed along Z direction) with (a) a section ABCD within which the crystallographic orientations of the grain of interest (GOI) and its neighbours are studied, and the grain of interest and twins within the GOI, where a few noticeable twins are labelled 1-7, (b) the IPFZ map of the section ABCD, and (c) Top (TV) and side views (SV1 and SV2) of GOI and twin of interest (TOI), which shows that the periphery of the TOI meets that of the GOI. The black ellipse indicates a discontinuity in the reconstructed twin caused by a malfunction of the EBSD detector and PQRS indicate the edges of the TOI.

In order to study the crystallographic orientation and thus the propensity of the GOI to twin, a section ABCD that cuts through the middle of the GOI is considered. Fig. 4(a) shows this plane, while the corresponding IPFZ map is shown in Fig. 4(b) along with the HCP unit cells that indicate the orientation of respective grains and twins. The IPFZ map shows the presence of extension twins within the GOI. This is expected as the loading is in the Z direction and the magnified view of the GOI shows that its crystallographic orientation is favourable for activation of extension twinning with its c-axis aligned away from the loading direction. Thus, the GOI is a classical case, where twins nucleate within a favourably oriented parent grain. Fig. 4(a) also shows around 19 twins (only 7 are labelled for the sake of clarity) within the grain of

interest, which makes it a suitable candidate for twin nucleation analysis. In order to study twin nucleation, it is preferable to identify the twin that nucleated first in the deformation history. This is necessary as it is argued in several independent studies that the local stresses and energy are relaxed/redistributed once a twin nucleates, which may then lead to the activation of other twins in the microstructure (Barnett et al. (2012), Liu et al. (2018), Paramatmuni et al. (2020)). In addition, other studies have also shown that once a lenticular twin forms (nucleation and propagation), it further accommodates strain by growing laterally (Qiao et al. (2016), Liu et al. (2019)). Therefore, in the current analysis, among the 19 twins shown in Fig. 4(a), the twin with the highest volume fraction is assumed to be that which nucleated first within the GOI. Table. 2 lists the volume fractions of the parent grain and the associated twins, where among the 19

Table 2: Summary of volume fractions of gain of interest

Volume fraction (%)		
Parent grain		86.18
Twins	**1**	**4.79**
	2	2.55
	3	0.78
	4	0.72
	5	0.70
	6	0.66
	7	0.58
	8	0.34
	9	0.34
	10	0.28
	11	0.23
	12	0.23
	13	0.20
	14	0.18
	15	0.18
	16	0.18
	17	0.16
	18	0.15
	19	0.10

twins, twin 1 has the highest volume fraction followed by twin 2. Therefore, the drivers for the nucleation of twin 1 are investigated in this study.

The top (TV) and side views (SV 1 and 2) of the grain of interest along with the twin of interest (TOI) are shown in Fig. 4(c) to study the shape of the latter. The black ellipse in the TV indicates a region of twin with an abrupt discontinuity on its surface. This is formed due to the lack of data for about 2 μm thickness caused by malfunctioning of the EBSD detector. The figure also shows points on the twin boundary indicated as P, Q, R and S. The preliminary observation is that the twin grows in the form of a plate in three dimensions and that the thickness along the twin surface normal is less than that in other directions, as observed in other studies (Liu et al. (2019)). Further, it appears that this twin has grown up to the periphery of the parent grain. From the TV, the edges QR and PS are indeed at the periphery of the parent grain. Further, the side views confirm that the edges PQ and RS also meet the parent grain at its periphery. In addition, from the side views (e.g. SV1) it is evident that the twin surface normal is inclined at an angle of 35.2° with the Z (loading) direction.

Of the six possible symmetric twin planes and directions shown in Table 3, the twin variant can be determined by the orientations method (Paramatmuni et al. (2020)) and/or by twin trace

Table 3: Extension twin variant types

Variant type	Crystallography
1	$(10\bar{1}2)[\bar{1}011]$
2	$(01\bar{1}2)[0\bar{1}11]$
3	$(\bar{1}102)[1\bar{1}01]$
4	$(\bar{1}012)[10\bar{1}1]$
5	$(0\bar{1}12)[01\bar{1}1]$
6	$(1\bar{1}02)[\bar{1}101]$

analysis (Jonas et al. (2011)). Here, the twin variants are arbitrarily called variants 1-6 for the sake of clarity as mentioned in Paramatmuni et al. (2020). Fig. 5(a) shows the crystallographic orientations as measured by EBSD and those calculated numerically that suggest the active twin to be variant 3, which is confirmed by the trace analysis in Fig. 5(b). For the sake of completeness, global Schmid factors, which rely on remote loading conditions, are also determined for all six twin variants, as shown in Table 4. From this analysis, variant 3 has the

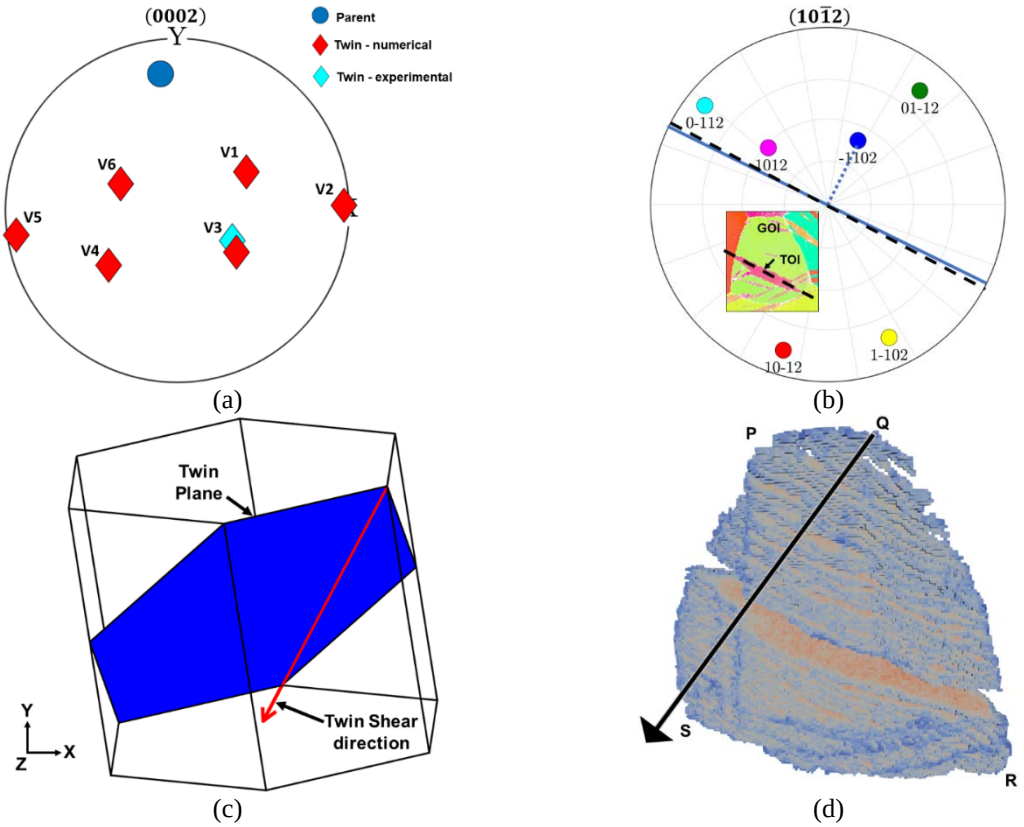

Figure 5: Twin variant type, twin plane and direction identification: (a) orientation method, where the basal pole figure shows discrete orientation of GOI, experimentally measured and numerically calculated TOI orientations (b) twin trace method, where the (10$\bar{1}$2) pole figure shows the twin plane poles and twin traces (c) the HCP unit cell along with the twin plane and direction corresponding to variant 3 and (d) the Top view of the TOI along with a projection of the independently calculated variant 3 twin direction on the XY plane, which shows that the twin may have nucleated at the vicinity of Q.

Table 4: Global Schmid factors of twins in the grain of interest

Euler angles			Variants					
Φ_1	Φ	Φ_2	1	2	**3**	4	5	6
7	111	5	0.20	-0.06	**0.30**	0.24	-0.06	0.26

highest global Schmid factor followed by variant 6 and 4. Therefore, the global Schmid factor also identifies the correct twin variant, again confirming that the TOI is, indeed, a classical twin. In summary, the selected TOI in the current study possesses the highest global Schmid factor among all the available six twin variants and also corresponds to that with highest volume (see Table 2). These observations agree well with other studies, which suggest that the classical twin with highest global Schmid factor nucleates first in the parent grain (Godet et al. (2006), Barnett et al. (2014), Wang et al. (2020)) and possesses a high rate of twin growth as

297 indicated by its global Schmid factor (Beyerlein et al. (2010), Paramatmuni and Kanjarla (2019)).
298 Thus, the TOI has, indeed, nucleated first in the GOI.

299 In order to study the local drivers of twin nucleation, it is necessary to locate the nucleation site
300 of the TOI without ambiguity. It is shown in Fig. 4(c) that all the twin edges (P, Q, R and S)
301 meet the parent grain at its periphery. As a consequence, it is challenging to identify the twin
302 nucleation site in the parent grain. However, extension twinning is a unidirectional 3D defect.
303 This implies that after a twin nucleates, it propagates along the twin shear direction only (hence
304 unidirectional) and later grows in the lateral directions. Thus determining the twin shear
305 direction in 3D is sufficient to locate the twin nucleation site. Therefore, the twin plane and
306 direction of TOI (variant 3) are first plotted in the {0,0,0} reference crystallographic
307 orientation, which are then rotated to the orientation of the GOI. Fig. 5(c) shows the plane and
308 the corresponding twin shear direction after rotation. This configuration of twin plane, when
309 viewed along the Z direction, is similar to that of the top view of twin in Fig. 5(c) , where the
310 twin at PQ grows into the GOI until RS. In addition, as mentioned earlier, the normal to the
311 twin surface is inclined at an angle of 35.2° with the Z (loading) direction. From the twin shear
312 direction in Fig. 5(c), the twin appears to have nucleated on the edge PQ. This is further
313 independently confirmed by rotating the $\langle 1\bar{1}01 \rangle$ twin direction of variant 3 to the orientation
314 of the GOI (see Guo et al. (2020) for the procedure) and then projecting this direction onto the
315 XY plane, as shown in Fig. 5(d) . This projection confirms that the twin direction is indeed the
316 vector originating at the vicinity of Q. Thus the TOI has indeed nucleated at the vicinity of Q
317 and propagated until the vicinity of S before growing laterally towards the P and R directions.
318 This is in line with a recent 3D study (Liu et al. (2019)), which suggests that the nucleated twin
319 initially propagates along the shear direction (in this case Q-S) and then grows in the lateral
320 directions (widens along P-R). In addition, from Fig. 5(c), considering the twin plane and twin

shear direction, the nucleation of the TOI is likely to be slip-assisted instead of being driven by an incoming twin from the neighbouring grain (twin-assisted twinning).

Fig. 6(a) shows the GOI along with neighbouring grains at the vicinity of Q as indicated by a black solid circle. The twin nucleation site appears to be at a triple junction, which is a preferred location as it is a source of high energy and defects necessary for twin nucleation (Abdolvand and Daymond (2013)). This is further corroborated in the grain boundary misorientation map shown in Fig. 6(b) of a section at some distance from the top surface. The vicinity of location Q is formed by a high angle grain boundary that favours slip-assisted twin nucleation, where the dislocation pileup dissociates to form a twin nucleus (Khosravani et al. (2015), Jeong et al. (2018)). This further confirms that the TOI is a typical example of slip-assisted twinning. In

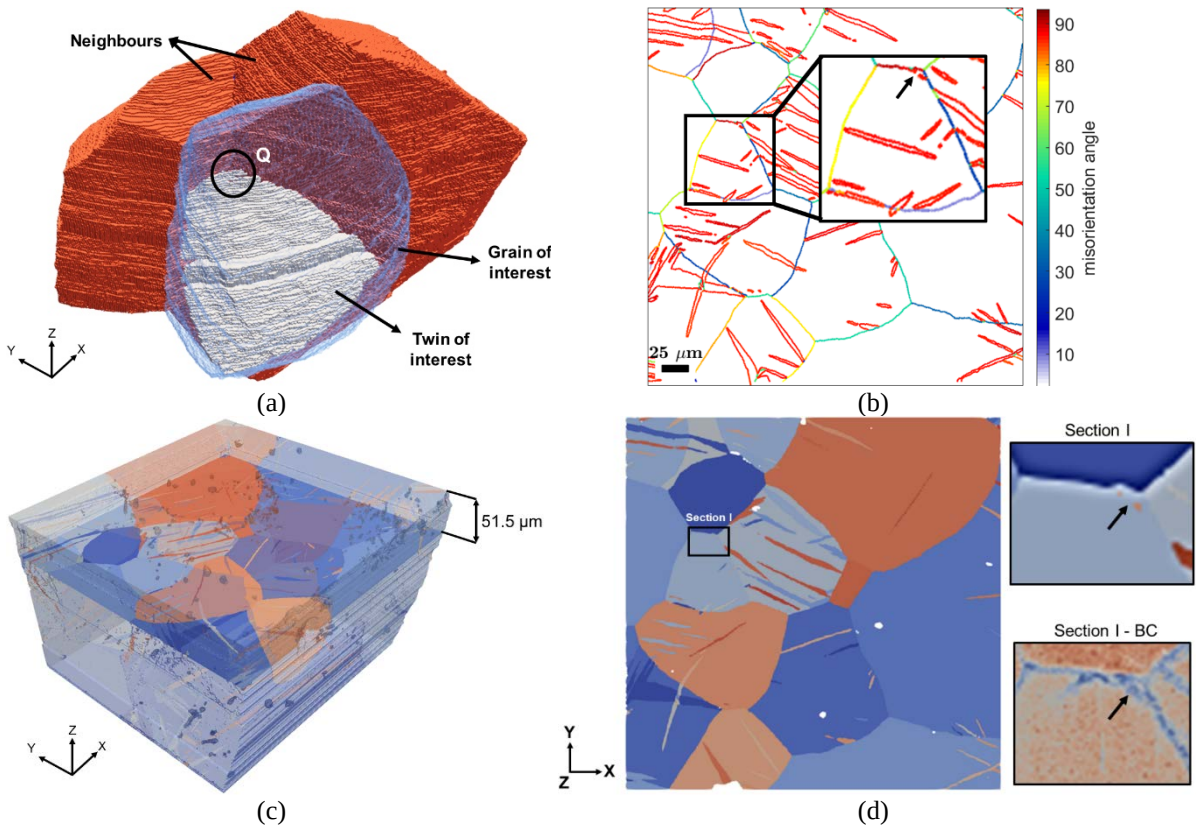

Figure 6: Investigation of the location of twin nucleation site (a) the 3D representation of the TOI, GOI and immediate neighbours of GOI, where the back circle indicates the tip of twin at the vicinity of Q that is close to the triple junction formed by these grains, (b) the grain boundary misorientation angle within a section of microstructure showing the tip of twin at the vicinity of Q, (c) the microstructure showing a section from a distance of 51.5 μm from the top surface, where the top tip of TOI is observed and (d) the detailed view of this section, where section I shows the magnified view of the twin. The band contrast (BC) map of section I shows a fully formed TOI band in 2D.

order to precisely locate the nucleation site, a plane containing the location Q is probed, which is at a distance of 51.5 μm from the top surface of the microstructure as shown in Fig. 6(c). This plane is shown in Fig. 6(d) along with the magnified view of section I that contains the location Q. The magnified view at the top is the microstructure coloured according to the feature IDs whereas the one at the bottom shows the band contrast (BC) map of the section I. While the feature IDs map shows an under developed twin, the respective BC map (bottom insert in Fig 6(d)) shows that this, in fact, is a fully developed twin that extends to the grain boundaries on either side. This implies that this section at a depth of 51.5 μm is not the precise location of the twin nucleation site.

It is shown thus far that the twin nucleation site lies in the approximate vicinity of location Q but at a depth less than 51.5 μm from the top surface. The microstructure in this vicinity is carefully investigated to locate the twin nucleation site. Fig. 7(a)-(c) show the BC maps of

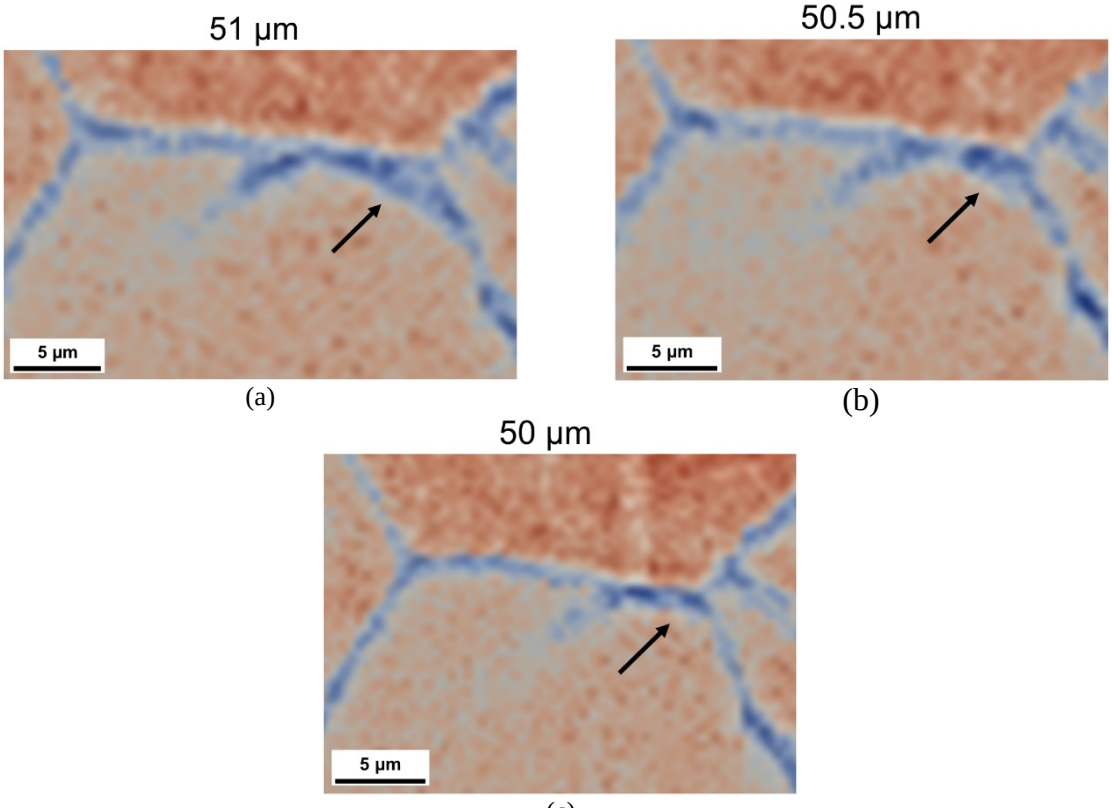

Figure 7: Band contract maps in the region of Q for sections lying at depths of (a) 51 μm, (b) 50.5 μm and (c) 50 μm from the top surface of the reconstructed 3D microstructure.

region-Q at a distance of 51 μm, 50.5 μm and 50 μm respectively from the top surface. The BC map at a depth of 51 μm shows a twin extended into the GOI, which is smaller than that at 51.5 μm. Although the map at 50.5 μm also shows a defect bulging into the GOI, it, however, cannot be unambiguously classified as a twin as the BC map at 50 μm also looks similar with a small protrusion into the GOI. These protrusions in Fig. 7(b) and (c) could either be the grain boundary itself or dislocation pileup developed to accommodate shear strain caused by the nucleation of twin, as observed elsewhere (Khosravani et al. (2015)). Therefore, the location of the twin nucleation site is thought to be at 51 μm, which is further addressed by investigating the local drivers of twin nucleation in the next section.

3.2 Crystal plasticity analysis of twin nucleation in 3D

Here we use modelling to better understand the drivers for the nucleation of the TOI within the GOI in the vicinity of Q. Previous studies (e.g. Qiao et al. (2016), Ardeljan et al. (2017)) have shown that classical twins nucleate when the positive twin resolved shear stress (TRSS : stress resolved on the twin plane along the twin shear direction) of a given variant at a particular location within the parent grain reaches a critical value. However, in these studies, either a local imperfection is introduced within the parent grain or other deformation fields such as the von Mises stress are typically employed to locate twins. Paramatmuni et al. (2020) have shown that the total stored energy density criterion naturally locates such twin nucleation sites without having to introduce any imperfections. For the crystal plasticity finite element modelling, it is necessary to establish the initial microstructure prior to the applied loading at which stage the grains are twin free. Of course as a destructive sectioning method, 3D-EBSD is not able to ascertain the grain microstructure before and after straining and so this must be estimated from the post-deformation 3D-EBSD characterisation. To do this, all the twins are subsumed within their parent grains and assigned the orientation of the latter to reflect the pre-twin state. Hence

367 the 3D-EBSD characterised microstructure containing twins shown in Fig. 8(a) is transformed
368 into the corresponding twin-free parent grains microstructure as shown in Fig. 8(b).

369 A sub region of the 3D microstructure with dimensions of 125x140x125 μm^3 as shown in Fig.
370 8(c) is used, where the GOI is surrounded completely by neighbouring grains. It is also ensured
371 that the GOI does not directly impinge surfaces to reduce any boundary effects. The sub region,
372 which consists of 12 grains shown in Fig. 8(c), is discretised into a total of 77,326 C3D20R
373 finite elements, with the GOI comprising 11,226 elements. This implies that the size of each
374 element is 3x3x3 μm^3, which governs the resolution of the current crystal plasticity analysis.
375 This FE model is loaded along the Z direction with periodic boundary conditions at strain

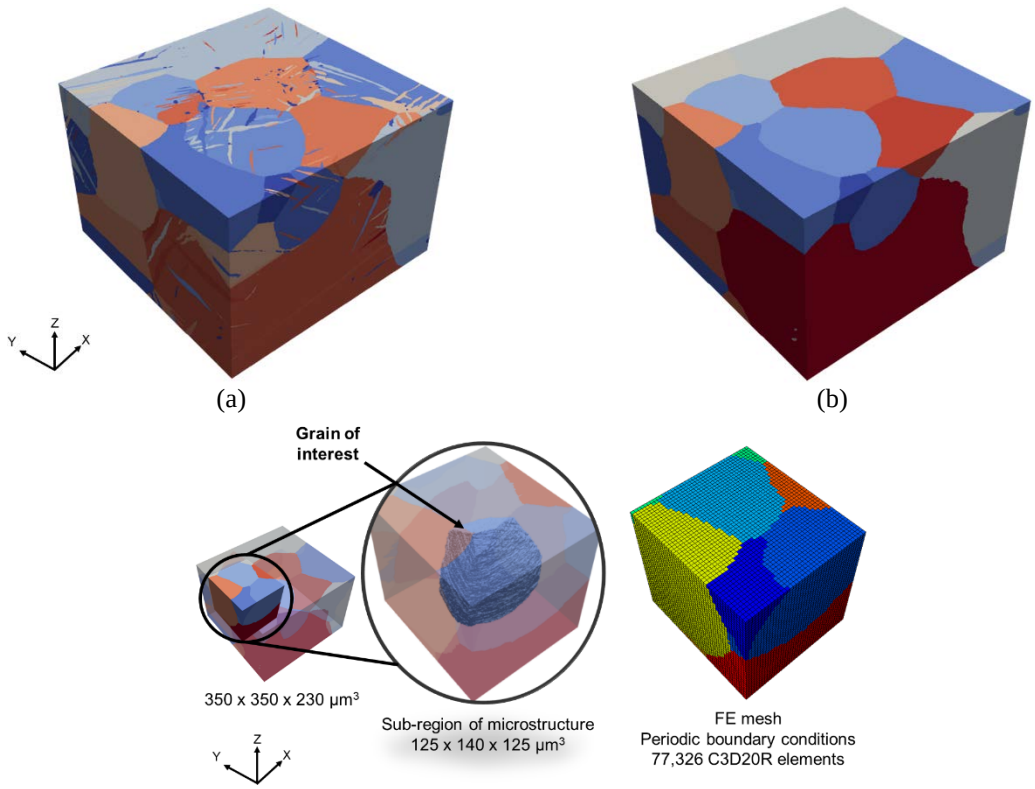

Figure 8: Simulation setup for the crystal plasticity analysis showing (a) the reconstructed microstructure cropped to a cube, (b) the microstructure in which the twins are merged into the respective parent grains to infer an initial undeformed microstructure and (c) the sub-region of microstructure, containing the grain of interest, considered for finite element crystal plasticity analysis.

376

377 rate of 0.002 s^{-1} until 1% strain. The material properties detailed in section 2.3 are used in the
378 simulation. The material crystallographic texture and the macroscopic loading condition are

379 favourable for the nucleation of twins. Thus the material deformation fields are first studied at
380 0.5% strain, which is closer to the macroscopic material yield point (nominal 0.2% strain).

381 Several types of boundary conditions (BCs) can be implemented in numerical analyses of
382 heterogeneous domains (RVEs) to understand the effective properties manifested by the local
383 deformation of materials. The commonly used BCs are the part-constrained ones (where only
384 one end of the RVE is constrained, while loading in the opposite end) (Zhang et al. (2015)), the
385 uniform displacement or Dirichlet, uniform traction or Neumann, Dirichlet-Neumann or mixed
386 ones (combination of displacement and traction) (Yue and Weinan (2007)) and the periodic ones
387 (e.g. Terada et al. (2000), Abdolvand et al. (2011)), which require the opposite faces of the RVE
388 deform in a similar manner. It is demonstrated in several studies that the mixed BCs, which are
389 more realistic, lead to better approximations of effective properties compared to that of the
390 uniform displacement and uniform traction BCs (Hill (1963)). Further, when considering
391 between the mixed and periodic BCs, Van der Sluis et al. (2000) in their detailed microscopic
392 analyses of a periodic structure suggested that the latter is more appropriate (also see Yue and
393 Weinan (2007)). Thus, in summary, implementing periodic BCs on a heterogeneous RVE with a
394 periodic structure leads to a better representation of the effective and microscopic properties.
395 However, Terada et al. (2000) have shown that for general heterogenous materials, periodic BCs
396 applied on a relatively small non-periodic RVE also provide reasonable trends of effective and
397 microscopic properties.

398 It has been shown by Paramatmuni et al. (2020) that the total stored energy density is a driver
399 for the nucleation of non-classical twins. Here, the spatial distribution of this energy density in
400 3D is investigated by measuring it along the perimeter of the GOI at depths of 15 μm, 30 μm,
401 45 μm, 51 μm, 60 μm, 75 μm, 90 μm and 105 μm as shown in Fig. 9. Table 5 shows the

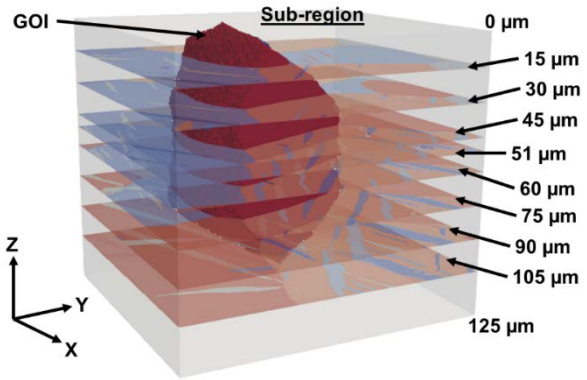

Figure 9: The sub-region of microstructure showing the planes at depths of 15 µm, 30 µm, 45 µm, 51 µm, 60 µm, 75 µm, 90 µm and 105 µm on which the deformation fields are measured along the periphery of the GOI.

microstructures, corresponding to the spatial distribution of stored energy density at 0.5% strain and the paths along the perimeters of the GOI that are used to measure the local total stored energy density. The qualitative analysis shows that the total stored energy density is low at the depths of 15 µm and 30 µm, increases between depths of 45 µm and 90 µm, and decreases at depths greater than 90 µm. Although the stored energy density between 60 µm and 90 µm depths is high, its magnitude along the grain boundaries appear lower than that within the grain. It has been established in other independent studies that the favourable locations for the slip-

Table 5 : The sections of microstructure showing the spatial distribution of the total stored energy density

Depth (µm)	Stored energy density (FE model)	Microstructure
15	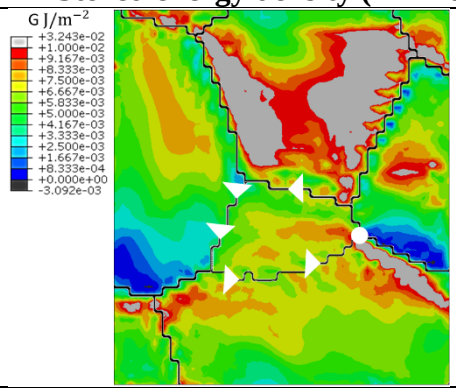	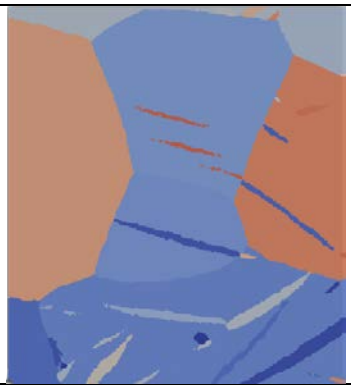

30		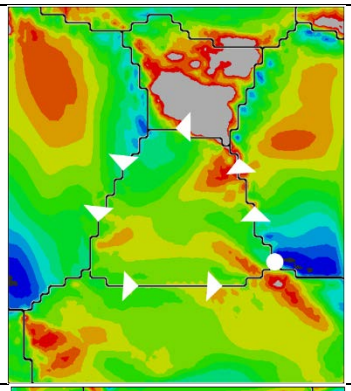	
45		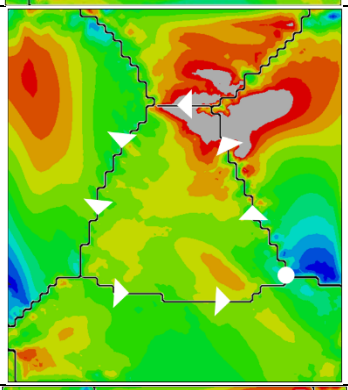	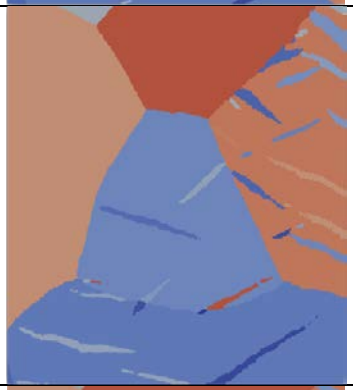
51		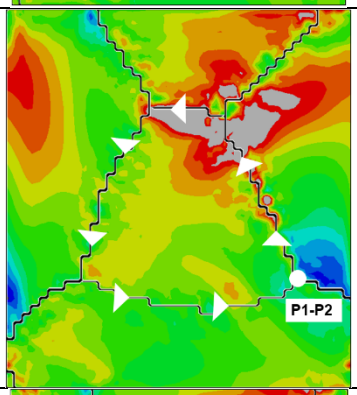	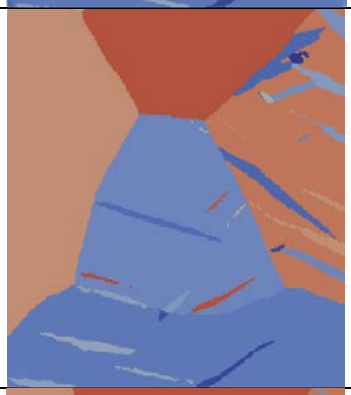
60		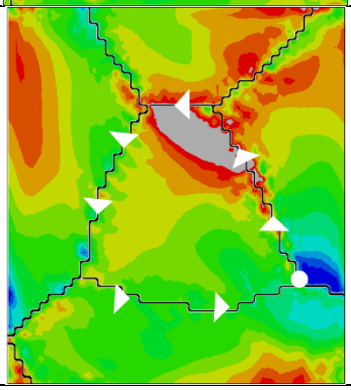	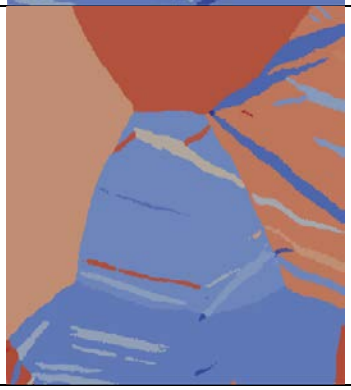

75	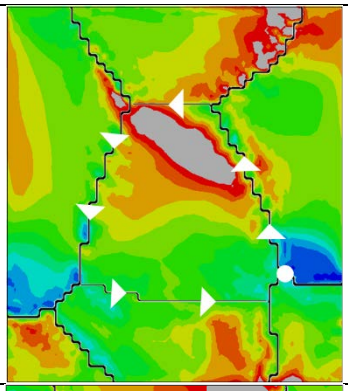	
90	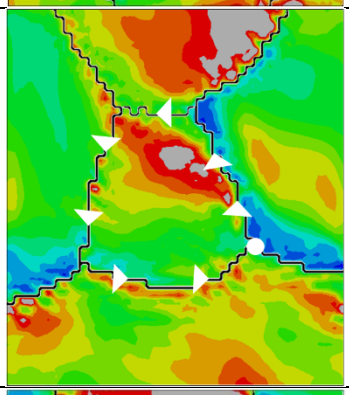	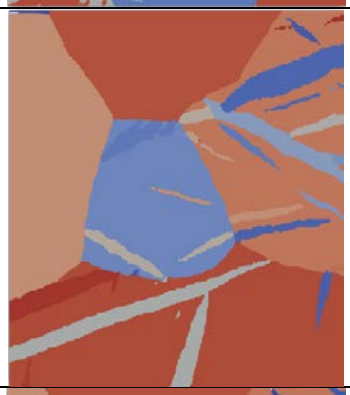
105	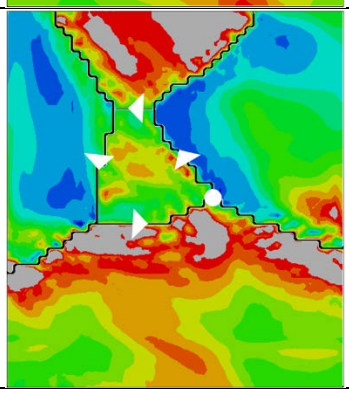	

Note : The arrows indicate the path along which the deformation field variables are measured. The dot indicates the start and end points of these paths. The numerical results correspond to total strain of 0.5%, while the corresponding experimental sections are obtained after deformation until 4% strain. In addition, note the development of the TOI at depths greater than 51 μm and the corresponding stored energy density at the grain boundary of the GOI. The qualitative observations indicate that the stored energy density at the grain boundary is high only at the depths of 51 μm, 45 μm and 60 μm.

assisted nucleation of twins are the grain boundaries (Beyerlein et al. (2010), Khosravani et al. (2015)) and that a twin nucleates within the parent grain when heterogeneities such as dislocation pile-ups lead to high local stresses. Thus from this qualitative analysis, it appears that the stored energy does not predict twin nucleation at depths greater than 60 μm, which is consistent with the earlier experimental analysis.

Fig. 10(a) shows the distribution of total stored energy density measured along the perimeters at different depths as shown in Table 5. The dashed line indicates the twin nucleation site at 51 μm as speculated in the earlier experimental analysis. From the figure, the peak value of total stored energy occurs at the depth of 51 μm, which coincides exactly with the speculated twin nucleation site (dashed line). Thus, the stored energy density analysis aids confirmations that the TOI did indeed nucleate at the triple junction at 51 μm from the top surface. Further, as mentioned earlier, the resolution of the current modelling is 3 μm. Thus, the stored energy is further investigated at the vicinity of 51 μm depth. Fig. 10(b) shows the stored energy measured along the periphery of GOI at depths of 45 μm, 48 μm, 51 μm, 54 μm and 57 μm. From this figure, the stored energy density at 48 μm is close to but still less than that at 51 μm. Further, as mentioned earlier, the numerical results at depths of 60 μm, 75 μm and 90 μm show hotspots

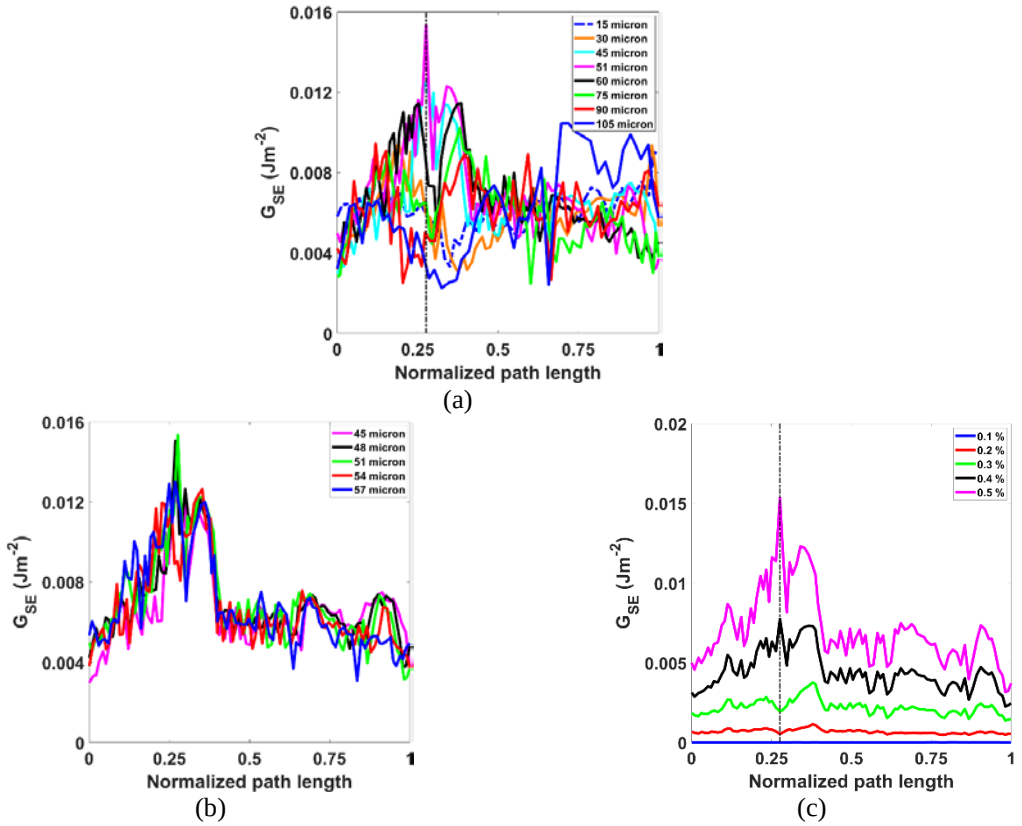

Figure 10: The total stored energy density spatial distributions: (a) measured along the GOI perimeters (paths shown in Table 5) at the depths indicated, where the dashed line indicates the twin nucleation site at 51 μm depth and (b) at depths of 45 μm, 48 μm, 51 μm, 54 μm and 57 μm and (c) the total stored energy density quantified along the path at 51 μm depth for strains of 0.1 % - 0.5 %.

of stored energy density within the GOI. The quantitative analysis, however, in appendix A demonstrates that the magnitude of these hotspots is less than that at a depth of 51 μm. This further establishes that the twin shear direction speculated earlier in Fig. 5(c) and (d) is indeed correct and that the TOI nucleated at the triple junction at 51 μm depth and propagated from Q in the direction of S and grew laterally in P and R directions.

It is reported that extension twins nucleate when the local total stored energy density reaches a *critical* value of the order 0.015 Jm^{-2} (Paramatmuni et al. (2020)). The maximum value of stored energy density at the twin nucleation site in Fig. 7(b) at 0.5% strain is 0.0158 Jm^{-2}, which is close to the reported *critical* stored energy density. This energy density is stored within local GNDs, the density of which may vary with the mesh element size (in general, the reference volume used to average the dislocation density (Arsenlis and Parks (1999)). However, Paramatmuni et al. (2020) demonstrated that, although the mesh size (reference volume) does affect the GND density, the order of magnitude remains the same (in their case, the magnitude of GND density for four different mesh sizes remained between 14 to 15 ($\log10(m^{-2})$)). This implies that the order of magnitude of the stored energy density determined locally remains the same for a range of mesh sizes. Thus it is suggested that the TOI nucleated at the *critical* stored energy density of the order 0.015 Jm^{-2} that occurs at 0.5% strain, which is further corroborated by the crystallographic orientation of the parent grain that is oriented favourably for activation of both basal slip and extension twinning. That is, although the parent grain orientation is favourable for the nucleation of extension twins, it first activates basal slip, which is then followed by extension twin nucleation. In addition, the global Schmid factor of the TOI is 0.30 (< 0.5), which implies that its nucleation occurs at strain levels greater than the nominal 0.2% yield strain. This is verified by extracting the stored energy at 51 μm depth from 0-0.5 % strain in steps of 0.1% applied average strain. Fig. 10(c) shows the stored energy from 0.1% -0.5%,

where the stored energy density at the twin nucleation site is less than the *critical value* at strains 0.1%-0.4%. The *critical value* is reached only at macroscale (average) strain of 0.5%.

While it is shown in independent studies that the von Mises stresses can locate twins (Ardeljan et al. (2017)), a few other studies have also reported high GND density at the vicinity of twin tips (Khosravani et al. (2015)). Thus the distribution of von Mises stresses, effective plastic strain and the GND density are investigated by measuring these quantities along the paths shown in Table 5. Fig. 11(a) shows the von Mises stresses at different depths of microstructure, where the dashed line indicates the twin nucleation site. From this figure, the von Mises stress is high both at 45 μm and 51 μm depths, which leads to ambiguity in locating the twin nucleation site. Similarly, Fig. 11(b) shows the distribution of effective plastic strain, where it

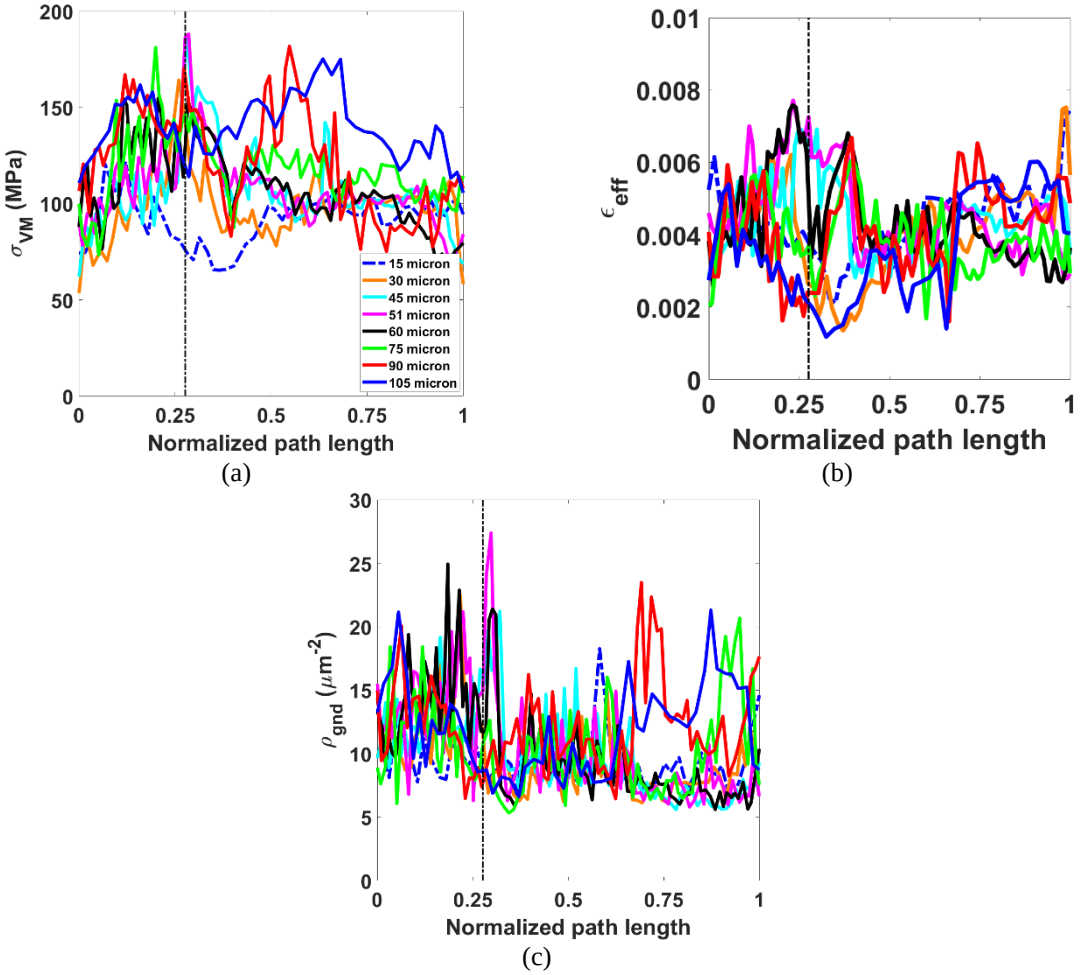

Figure 11: The distribution along the path at 51 μm as shown in Table 5 for (a) von Mises stress, (b) effective plastic strain and (c) GND density, where the dashed line indicates the twin nucleation site.

462 is high at the vicinity of, and not precisely at, the twin nucleation site at 51 μm and 60 μm. In
463 addition, the plastic strain is also high at the normalized distance of 1 at 15 μm and 30 μm
464 depths. Thus the effective plastic strain also leads to ambiguity in locating the nucleation site.
465 The distribution of GND density in Fig. 11(c) shows interesting trends, where the GND density
466 is high near the twin nucleation site at depth of 51 μm. Therefore, although the von Mises
467 stress, effective plastic strain and GND density appear relevant for twin nucleation, they do
468 not, in their own right, predict twin nucleation sites, similar to observations in the 2D analyses
469 of Paramatmuni et al. (2020). In addition to the above deformation fields, the twin resolved
470 shear stress is typically used to explain twin nucleation, which is now studied in detail.

471 Fig. 12(a) and (b) show the distribution for TRSS of all six twin variants, where the local stress
472 within the parent grain is resolved on six available twin planes and twin directions, along the
473 paths at depths of 51 μm and 45 μm respectively. The TRSSs of variants 2 and 5 are consistently
474 lower than the other variants, while the variants 3 and 6 possess highest TRSSs. The

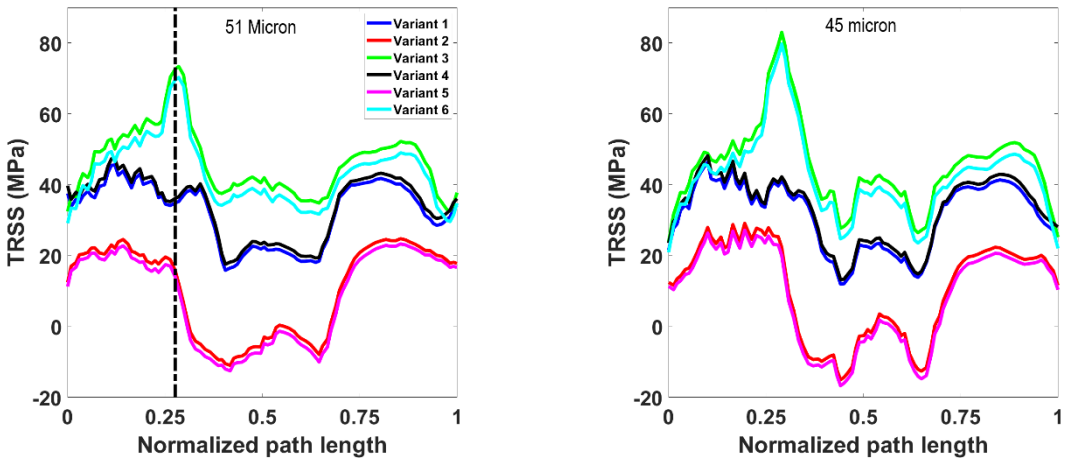

(a) (b)

Figure 12: The predicted distributions of TRSS measured along the GOI perimeters for each of the six twin variant types at depths of (a) 51 μm and (b) 45 μm, where the dashed line in (a) indicates the twin nucleation site.

475 experimental analysis shows that the variant 3 is active within the GOI. At 51 μm, the TRSS
476 for variant 3 is clearly the highest, which agrees well with the experimental observations.
477 However, the variants 3 and 6 show higher TRSSs at 45 μm compared to that of 51 μm. This

implies that the TRSS criterion predicts the twin nucleation to occur at 45 μm, which is in conflict with the experimental evidence. Thus the TRSS criterion alone does not appear to satisfactorily explain twin nucleation. However, from Fig. 10(a), the total stored energy shows that the twin nucleates at 51 μm without any ambiguity. While this only explains the twin nucleation, employing the TRSS criterion at 51 μm (where the twin is shown to nucleate) shows that variant 3 has the highest TRSS, which is selected by the parent grain. Therefore, from these analyses, the total stored energy density criterion locates the twin nucleation site within the parent grain, while the TRSS criterion explains the variant selection.

4. Discussion

The crystal plasticity analysis shows that, while the effective plastic strain, von Mises stresses and GND density are relevant to twin nucleation, they do not precisely locate the twin nucleation site. It is shown that the total stored energy density, which is the fraction of plastic energy that is stored in the material in the form of local dislocation structures, precisely locates the twin nucleation site. This is reasonable as this criterion considers both the localization of stresses (energy) and defects (dislocations) necessary for the nucleation of twins. Thus the present results in conjunction with the previous work of Paramatmuni et al. (2020), show that the stored energy criterion is necessary to predict the nucleation sites of both classical and non-classical twins.

It is speculated in Paramatmuni et al. (2020) that in the case of classical twins, the TRSS criterion may dominate over the total stored energy density while locating the twin nucleation sites. The present study confirms that the stored energy density criterion is necessary to locate the twin nucleation site, while the TRSS criterion explains the variant selection. In addition, it is also shown in Paramatmuni et al. (2020) that the shear stored energy density (S_{SE}), which is a measure of that energy stored within the embryo of a potential active twin nucleus, predicts

the active twin variant. According to this criterion, in the case of non-classical twins, the twin variant that possesses minimum energy of formation is selected by the parent grain. On a continuum scale, this energy was approximated to be equivalent to shear stored energy density on a given twin variant β that depends on the local TRSS (τ^{β}), resolved plastic shear strain (γ_P^{β}) and local dislocation structures as shown in equation (8) (Paramatmuni et al. (2020)).

$$S_{SE} = \frac{\tau^{\beta}\,\gamma_P^{\beta}}{\sqrt{\rho_{SSD}+\sum_{i=1}^{n}\rho_{GND}^{i}}} \tag{8}$$

This criterion is now investigated by measuring the S_{SE} along the path at depth of 51 µm shown in Table 5. Fig. 13 shows the distribution of S_{SE}, where it is least for variant 4 and highest for variant 3. The energy density is high for variant 3 since its local TRSS, which is the highest among all six variants as shown in Fig. 12(a), dominates the local energy density. This shows

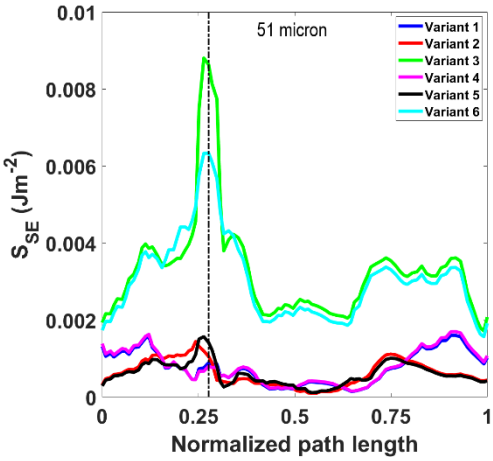

Figure 13: The distribution of the shear stored energy density (S_{SE}) along the GOI perimeter on a section at a depth of 51 µm from the top surface.

that the S_{SE} criterion proposed earlier seems not to explain variant selection in the case of classical twins. It is to be noted that the TOI in this work is indeed classical and that it nucleated within a parent grain well oriented for nucleation of twins. This implies that, in classical twins, the TRSS criterion is sufficient to explain variant selection at a given twin nucleation site, which is correctly located by the total stored energy density. Thus in summary, the current

518 analysis confirms that the stored energy density is necessary to locate twin nucleation sites in
519 both classical and non-classical twins. Further, while the S_{SE} criterion explains the variant
520 selection in non-classical twins, the TRSS criterion does so in the case of classical twins.

521 It is shown in Appendix A that the magnitudes in hotspots of total stored energy density at
522 depths of 60 μm, 75 μm and 90 μm within the GOI are less than the critical value for twin
523 nucleation reported in the current study. However, the numerical results in table 5 also show
524 high localized spots of stored energy density within neighbouring grains. In order to investigate
525 the magnitudes at these locations, the stored energy density is measured along specific paths
526 within neighbouring grains as shown in Appendix B. Among all the measured distributions in
527 Table B1 of Appendix B, the stored energy density exceeds the critical value within two grains
528 – grain Q at a depth of 15 μm and grain P at a depth of 30 μm. These distributions and their
529 implications are now investigated in detail. It is noted that the small-scale pillar is deformed to
530 4% strain as mentioned in section 2.2, while the numerical analysis is conducted until 1%
531 strain. The numerical results at 0.5% strain and the experimental results at 4% strain are shown
532 together in table 5 to indicate that the stored energy density reaches the critical value only at
533 51 μm, where the TOI is expected to nucleate. It is, however, consistently lower than the critical
534 value at the boundary of GOI at depths greater than 51 μm. Therefore, the presence of high a
535 density of twins within the GOI (except the TOI) and the neighbouring grains that possess
536 lower stored energy density in Table 5 (e.g. observe high density of twins in experimental
537 microstructure and corresponding lower stored energy density at the depth of 75 μm), implies
538 that these twins are formed at higher strains (>1%) when the corresponding local stored energy
539 density reaches the critical value.

540 Fig. 14(a) shows the section of 3D microstructure containing grain Q and the path AB along
541 which the distribution of total stored energy density is measured. This distribution is shown in
542 Fig. 14(b), where the dashed line in the figure indicates the critical value for twin nucleation

observed in this study. Here, the path begins at the vicinity of the RVE surface, where the boundary effects are significant, and ends at the grain boundary. From Fig. 14(b), the total stored energy density increases as the path progresses from the grain interior (close to the RVE surface) towards the grain boundary, where it exceeds the critical value. This implies that the current numerical analyses predict the presence of a twin at the boundary of grain Q at a

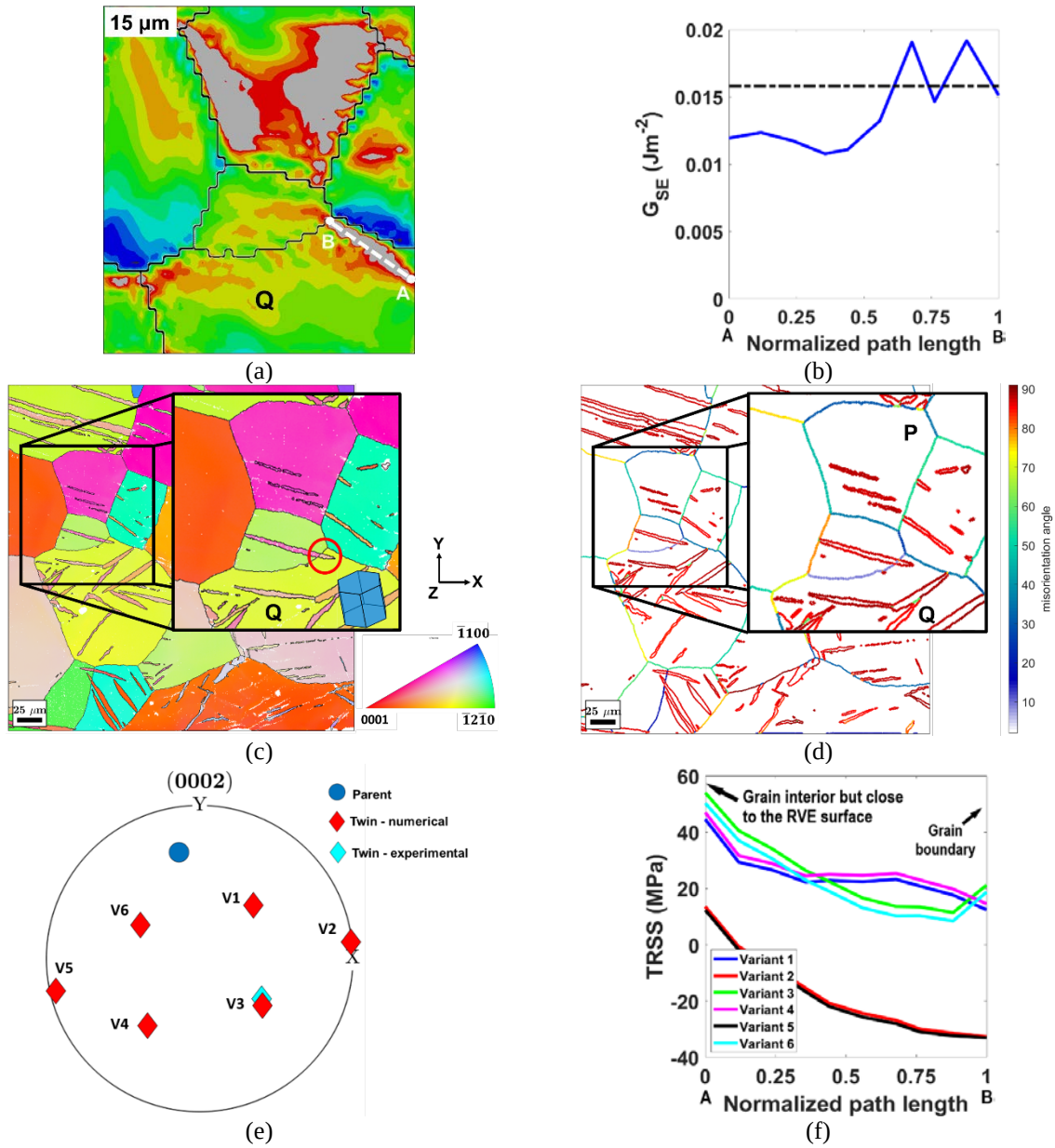

Figure 14: Twin nucleation analyses for grain Q showing (a) the spatial distribution of the total stored energy density at the depth of 15 µm and the path AB along which the energy density is measured, (b) the distribution of the total stored energy density along path AB, where the dashed line indicates the *critical value* of the energy density reported in the current study, (c) the IPF map showing the microstructure for a section of grain Q and the twin of interest at 15 µm depth, (d) the grain boundary misorientation map of the microstructure, (e) the orientation analysis of the TOI in grain Q and (f) the distribution of TRSSs of all six twin variants along the path AB

depth of 15 μm. In order to confirm this further, the microstructure at 15 μm depth is investigated in Fig 14(c) and (d). Fig. 14(c) shows the IPF map of this microstructure, where the hexagon indicates the crystallographic orientation of grain Q. This figure clearly shows the presence of a twin at the boundary within grain Q, where the total stored energy exceeds the critical value in Fig. 14(b). In addition, the figure also shows the presence of a twin in the adjacent grain, indicating a twin-assisted twin nucleation event. It is reported in other studies that a grain boundary misorientation angle less than ~35° promotes twin-assisted twin nucleation (Beyerlein et al. (2010), Khosravani et al. (2015)). The grain boundary misorientation angles within the microstructure at a depth of 15 μm are shown in Fig. 14(d). From this figure, the boundary misorientation angle of grain Q at the location of interest is ~15°, which is favourable for twin-assisted twin nucleation. Thus, it appears that the twin within grain Q nucleated when the local total stored energy density reached the critical value, which may have then nucleated a twin within the adjacent grain. Therefore, this analysis, similar to a previous study (Paramatmuni et al. (2020)), confirms that the total stored energy density also locates the sites of twin-assisted twin nucleation events.

The next step after locating the twin nucleation site is the prediction of the active twin variant. The active twin variant in this case is identified using the orientation analysis as shown in Fig. 14(e), where the analysis shows that the twin within grain Q belongs to variant type 3. Fig. 14(f) shows the TRSSs measured along the path AB (Fig. 14(a)) of all the available six variants. From this figure, the TRSS of variant 3 is the highest at the vicinity of the grain boundary. Thus, the current numerical analyses precisely locate the twin nucleation site and predict the active twin variant in grain Q.

The next location of interest with high total stored energy density lies within grain P at a depth of 30 μm as shown in Fig. 15(a). The total stored energy density measured along the perimeter of grain P is shown in Fig. 15(b), where the dashed line indicates the *critical value* of energy

density. From this figure, the total stored energy density reaches the critical value at the triple junction. However, the corresponding microstructure (IPF map) in Fig. 15(c) shows a twin located away from the triple junction. As shown in the orientation analysis in Fig. 15(d), this twin belongs to the variant type 3. In addition, the location of high total stored energy density

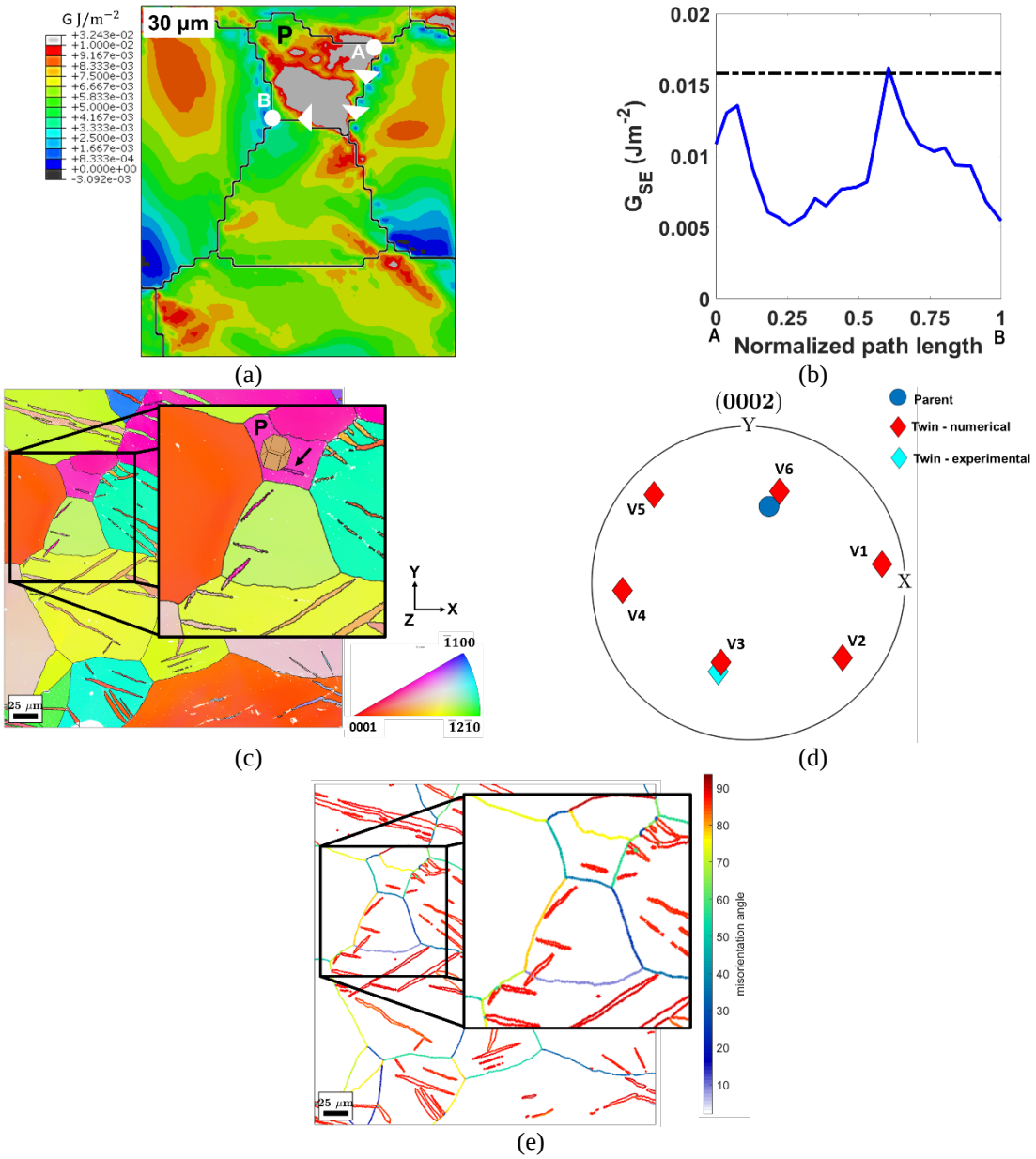

Figure 15: Twin nucleation analyses for grain P showing (a) the spatial distribution of the total stored energy density at the depth of 30 µm and the path AB along which the energy density is measured, (b) the distribution of the total stored energy density along path AB, where the dashed line indicates the *critical value* of the energy density reported in the current study, (c) the IPF map showing the microstructure for a section of grain P and the twin of interest at 30 µm depth, (d) the orientation analysis of TOI in grain P and (e) the grain boundary misorientation map of the microstructure.

578 is at the vicinity of a high angle boundary (~60°) within grain P as shown in Fig. 15(e). In
579 summary, there appears to be a discrepancy between the twin nucleation site as predicted by
580 the stored energy density criterion and experimental observation of the twin. However, as the
581 observed twin is located at the vicinity of the triple junction, it may have indeed nucleated at
582 the triple junction either over or under the depth of 15 µm. From table 5, while the total stored
583 energy density within grain P is less than the critical value at the depth of 15 µm, it is closer to
584 the critical value at 45 µm. Thus, the 3D volume is investigated further at depths >30 µm to
585 understand the discrepancy between the experimental observations and numerical analysis
586 observed at the depth of 30 µm.

587 Table 6 shows the IPF maps, the spatial distribution of the total stored energy density, and the
588 latter measured along the specified paths at the depths of 33 µm and 36 µm respectively in two
589 columns. The last row shows the TRSSs of all six twin variants measured along the path AB at
590 the depth of 36 µm. From the microstructures in Fig. 15(c) and first row of table 6, it is evident
591 that the twin lamella develops closer to the triple junction with an increase in depth, which
592 suggests that the twin may have, indeed, nucleated at the triple junction. While the

Table 6 : Twin nucleation analyses of grain P at depths of 33 µm and 36 µm.

	33 µm	36 µm
IPF Map	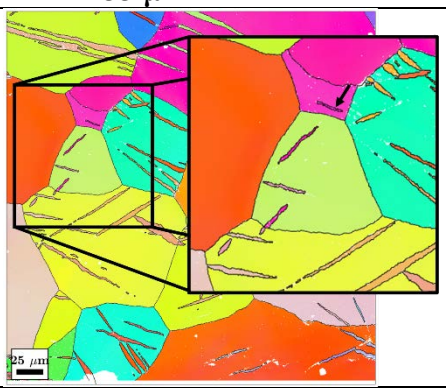	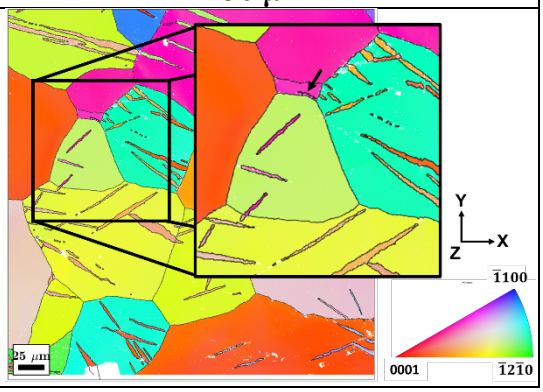

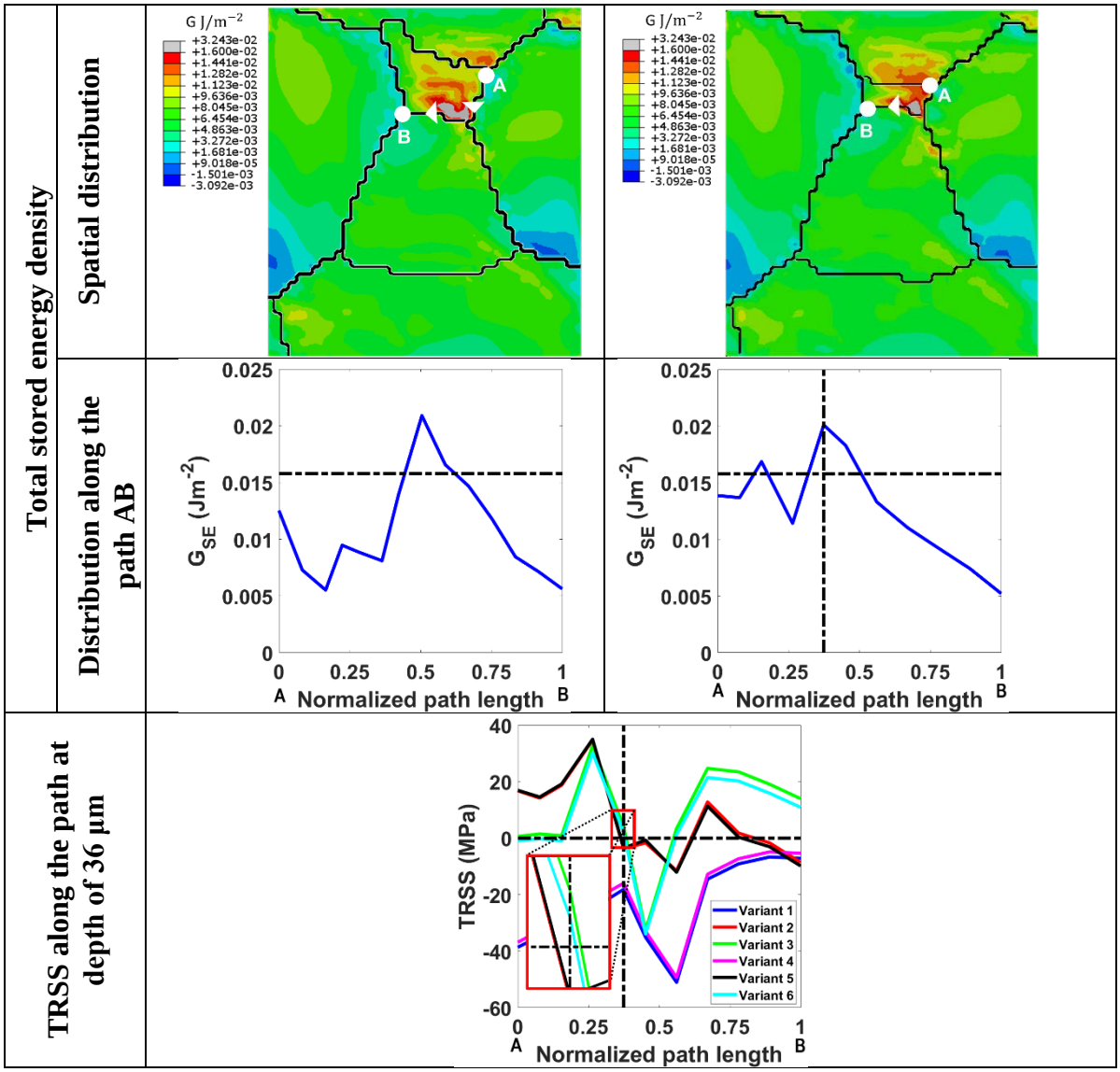

microstructure at 33 µm shows a fully developed twin away from the triple junction, that at 36 µm shows the twin tip located at the triple junction. Thus, this twin may have nucleated at the depth of ~36 µm. The spatial distribution of total stored energy density at depths of 33 µm and 36 µm show high stored energy density at the triple junction of interest (note that the maximum value in the scale is limited to a energy density value of 0.016 Jm^{-2}). Table 6 also shows the energy density measured along the paths AB, which confirm that the energy densities at these depths are higher than the *critical value*. Thus, this analysis confirms that the twin nucleated at a depth of ~36 µm. As twin nucleation is a local plastic relaxation phenomenon, if the

progressive twin formation were to be included, it is feasible that the nucleation of the twin at 36 μm would relax and redistribute the total stored energy density at 33 μm and 30 μm depths.

Further, in order to assess the variant selection, the TRSSs of all six twin variants are measured along path AB at 36 μm depth, which is shown in the last row of table 6. The vertical dashed line in this figure indicates the location corresponding to high total stored energy density. The magnified view shows the distribution of TRSSs at this location of interest. From this figure, while only variants 3 and 6 possess positive TRSSs, the TRSS of variant 3 is greater than that of variant 6. Thus, the numerical analysis predicts the activation of variant 3, which is in line with the experimental observations made in Fig. 15(d). Thus, these analyses further indicate that while the total stored energy density criterion successfully predicts slip-assisted nucleation of twins, the TRSS criterion predicts the active classical twin variant at depth of 36 μm within grain P.

Thus, it is now demonstrated in three independent cases that the total stored energy density precisely locates the classical twin nucleation sites. The GOI investigated in table 5 and the grain P provide strong evidence that it is absolutely necessary to study the nucleation of twins in 3D. For instance, considering only the 2D numerical results of grain P at a depth of 30 μm would lead to incorrect prediction of the twin nucleation site. Similarly, locating the approximate site of twin nucleation within the GOI in Fig. 7 required detailed analysis of a few sections of 3D reconstructed microstructure. This implies that while the 2D analyses are only indicators and provide some understanding of twin nucleation, they neither lead to precise location of the twin nucleation sites nor provide mechanistic insights into their formation. This is in-line with other numerical studies that demonstrated the importance of studying the 3D microstructure to understand the evolution of local deformation variables (e.g. Zhang et al. (2015)). In summary, the current study demonstrates that it is necessary, where possible, to investigate twin nucleation in 3D by integrating numerical with experimental analyses.

627 The crucial aspect in understanding microscopic properties within a given grain is the boundary
628 effects imposed by the neighbouring grains. These effects could either be soft, that is the
629 neighbouring grains are allowed to deform independently or hard, where the neighbouring
630 grains impose boundary effects on the grain of interest (Zhang et al. (2015)). The former is
631 achieved by using the part-constrained BCs, while the latter is achieved using the uniform
632 displacement (planar) BCs. Recently Zhang et al. (2015), in their crystal plasticity finite
633 element framework, demonstrated that the hard BCs satisfactorily reproduce the experimental
634 lattice reorientation. The periodic BCs are more realistic, which vary with the local
635 heterogeneity within the RVE (e.g. Kumar et al. (2006), Zhang et al. (2007), Heripre et al. (2007),
636 Abdolvand et al. (2011)).

637 In order to understand the effect of BCs, the sub-region of microstructure shown in Fig. 8(c) is
638 subjected to uniform displacement (planar) BCs as shown in Fig. 16(a). Fig. 16(b) shows the
639 spatial distribution of stored energy density at 0.7% strain at a depth of 51 μm, where the twin
640 is shown to nucleate within the GOI. The qualitative observations show two hotspots, D and
641 C, of the total stored energy density within the GOI. In order to understand this distribution,
642 the energy density is measured along the path indicated in Fig. 16(b), which is similar to that
643 shown in table 5 at depth of 51 μm. Fig. 16(c) shows the distribution of the energy density,
644 where it is higher than the critical value at both the locations D and C. The distribution of the
645 TRSSs of all six twin variants along the path indicated in Fig. 16(b) is depicted in Fig. 16(d).
646 This distribution, which is strikingly similar to that in Fig. 12, clearly shows that the TRSS of
647 variant 3, which is the experimentally observed active twin variant, is highest at location D
648 compared to that of C. That is, both the twin nucleation and the variant selection are driven
649 more at location D. If progressive twin formation were to be considered explicitly, the
650 formation of a twin at location D would relax and redistribute the energy density at location C,
651 as twin nucleation is a stress relaxation phenomenon. Thus, the planar uniform displacement

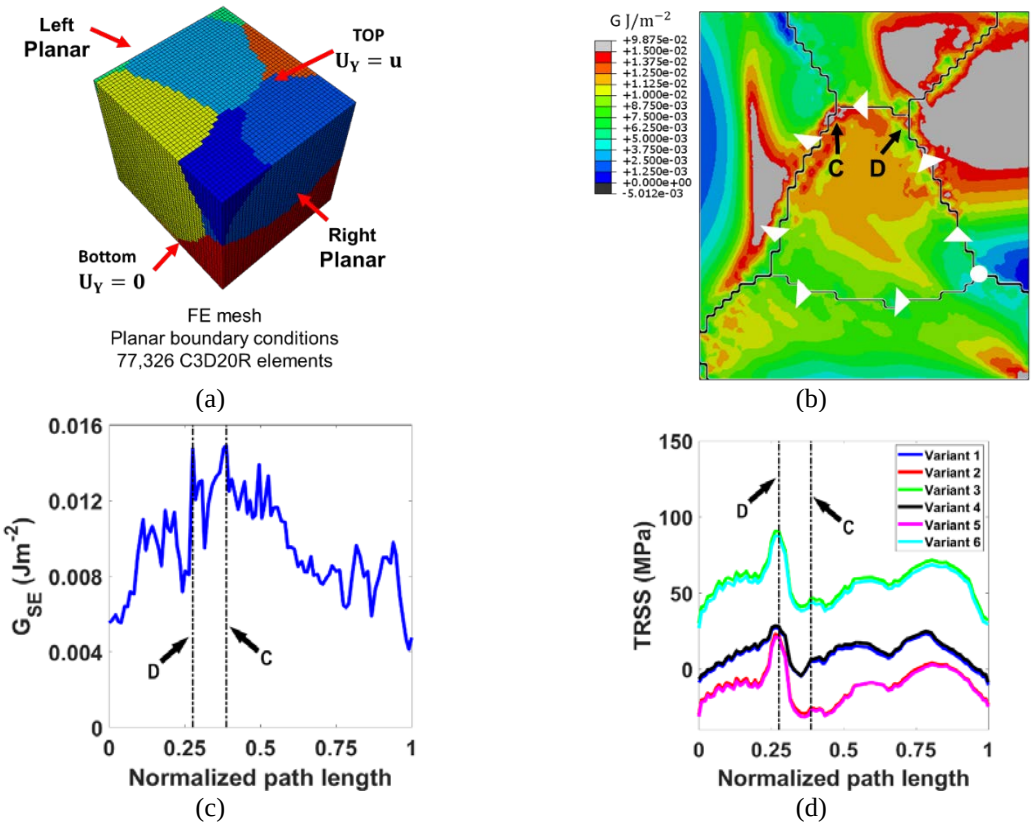

Figure 16: Twin nucleation analyses within the GOI using uniform displacement (planar) boundary conditions showing (a) the RVE and the applied boundary conditions, (b) the spatial distribution of the total stored energy density at a depth of 51 μm at 0.7% strain, where D and C indicate hotspots of energy density within the GOI, (c) the distribution of the energy density along the path and (c) the distribution of TRSSs for all six twin variants along the path shown in (b).

652

653 BC also predicts the twin nucleation at the same location as that of periodic BCs. However,
654 while the former predicts the nucleation to occur at 0.7% strain, the latter does so at 0.5% strain.
655 These differences in the numerical results are expected as the BCs have considerable influence
656 on the interaction between the GOI and its neighbours.

657 The current study shows that the TRSS criterion is sufficient to explain twin variant selection
658 in the case of classical twins. However, the magnitude of the TRSS of variant 3 within the GOI
659 (Fig. 12) at the twin nucleation site is ~75 MPa, which is about 2-3 times the CRSSs (25-40
660 MPa) reported elsewhere (Liu et al. (2017), Paramatmuni and Kanjarla (2019), Jeong et al. (2018)).
661 In addition, other studies have also shown that the yield stress (and therefore the CRSS) in
662 twinning dominated yielding decreases with an increase in grain size (Barnett et al. (2012)).
663 These observations imply that for the grain size (55 μm) of the material used in the current

study, much lower magnitudes of TRSSs should be expected. However, the previously reported CRSSs values are averaged single crystal properties. The TRSSs reported here are local and at the periphery of the GOI, which are high due to the highly localized accumulation of material defects at grain boundaries that result in high local stresses.

This effect, and that of grain boundaries, is investigated by simulating uniaxial compression of a micropillar, which is devoid of any heterogeneities such as grain boundaries. In a micropillar, the heterogeneous deformation, if any, is typically due to the geometry or inherent deformation behaviour of the material. A pillar FE model, comprising 2904 elements, with square cross section of size 5 μm, taper angle 2° and an aspect ratio of 1:2.6 is used, which is similar to other independent experimental studies (e.g. Jeong et al. (2018)). Fig. 17(a) shows this pillar supported by a single crystal base with the same crystallographic orientation. This micropillar and the base are assigned the material properties shown in section 2.3 and the crystallographic orientation of the GOI. It is loaded along the Z direction in compression at the strain rate of 0.001 s^{-1} to 2% strain. The accumulated total stored energy density during deformation reaches a critical value at macroscopic strain of 0.8% and at σ_{33} (macroscopic stress along the loading direction) of 80 MPa. Fig. 17(b) shows the spatial distribution of stored energy density and Fig. 17(c) the TRSS of variant 3, and the path XY in Fig. 17(b) along which these quantities are measured. The figure also shows heterogeneous deformation with high localisation of stored energy density and TRSS on the surface of the pillar. This is consistent with other studies that reported the nucleation of twins on the free surface of micropillars (e.g. Liu et al. (2017)). Fig. 17(d) and (e) show the distribution of stored energy density and TRSSs of all six variants respectively along the path XY, where the dashed line indicates the location of high stored energy density that is greater than the *critical value* of 0.015 Jm^{-2}. Fig. 17(e) shows that variants 3 and 6 possess high TRSSs compared to other variants. At the high stored energy density location, the TRSS of variant 3 is ~40 MPa, while that of variant 6 is ~36 MPa. These TRSSs

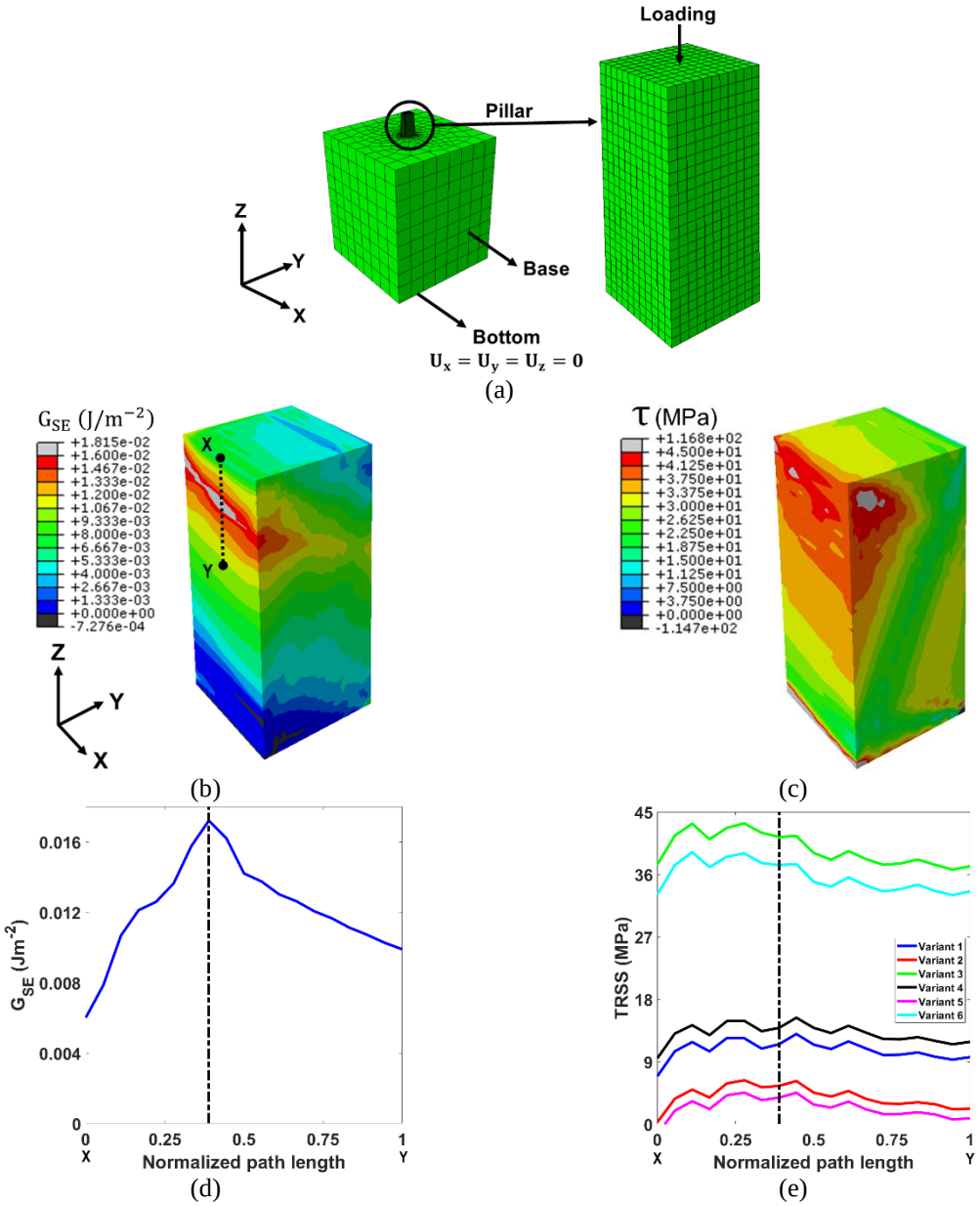

Figure 17: The single crystal deformation analysis showing (a) the isometric view of pillar configuration and magnified view of the pillar, the spatial distribution of (b) total stored energy density and (c) the TRSS of variant 3, where the path in (b) indicates that along which the (d) total stored energy density and (e) TRSS of all six variants are measured.

are greater than the CRSSs reported in independent experimental studies (Liu et al. (2017), Jeong et al. (2018)). However, these experimental studies typically report average CRSSs as opposed to the local TRSSs shown in Fig. 17(e). In order to put the current results in the context of the literature, the average TRSS (TRSSs in elements averaged over the entire micropillar in Fig. 10(a)) at 0.8% strain is determined for variant 3, which is found to be 29.2 MPa which is close to the CRSSs of 29 MPa (Liu et al. (2017)) and 32 MPa (Jeong et al. (2018)) reported in

other experimental studies. Further, the maximum stored energy density in Fig. 17(d) is 0.017 Jm^{-2}, which is close to the stored energy density of 0.0158 Jm^{-2} at the twin nucleation site in Fig. 10(a). For these similar stored energy densities reported in the single crystal (Fig. 17(d)) and polycrystal (Fig. 10(a)) settings (for the same crystallographic orientation), the corresponding TRSSs are ~40 MPa and ~75 MPa respectively. This suggests that the TRSS magnitudes reported in Fig. 12(a) are high as a consequence of grain boundary effects and local constraint but, as the analysis above shows, are completely consistent with the independent measurements of *average* TRSSs values in the literature.

5. Conclusions

In summary, we have undertaken a 3D investigation based on 3D-EBSD of deformed micropillars and crystal plasticity modelling to better understand the environment leading to twin nucleation. Our experimental and modelling results show a high degree of alignment and suggest that the total stored energy density can precisely locate the twin nucleation site in the case of classical twins, where the nucleation is driven by local dislocation structures in favourably oriented parent grains. Further, based on the evolution of stored energy density with deformation history and the parent grain orientation, it is observed that these classical twins nucleate at a *critical* stored energy density of the order 0.015 Jm^{-2}, which is similar to that of the non-classical twins. It is shown that the variant selection in the case of classical twins is driven by the local resolved stresses instead of the previously shown shear stored energy density, which explains variant selection in non-classical twins. However, the orientation of the parent grain in the current study is such that it nucleates basal slip before the extension twin and the global Schmid factor of the twin is ~0.3. The extreme case in this scenario is the orientation of a parent grain that is favourably oriented only for extension twinning, where the global Schmid factor is ~0.5. In such cases, where the parent grain preferentially activates extension twins before slip, the validity of the stored energy criterion needs to be explored. In

addition, the availability of 3D information of twins allows detailed investigation of twin growth and variants selection, which may form scope of future work.

Acknowledgements

C. P would like to acknowledge the award of Imperial College President's generous PhD scholarship. C. P also thanks Justine A. Delage, Department of Materials, Imperial College London, for their help in small-scale pillar compression. F. P. E. D acknowledges his Royal Academy of Engineering/Rolls-Royce research chair funding. P. J. W acknowledges support from the European Research Council grant No. 695638 CORREL-CT. This work was also supported by the Henry Royce Institute for Advanced Materials, funded through EPSRC grants EP/R00661X/1, EP/S019367/1, EP/P025021/1 and EP/P025498/1.

Appendix A. The distribution of total stored energy density within the grain of interest at depths of 60 μm, 75 μm and 90 μm

Table 5 shows hotspots of total stored energy density within the grain of interest (GOI) at the depths of 60 μm, 75 μm and 90 μm. In order to investigate the magnitudes at these depths, the energy density is measured along three additional paths that pass through these hotspots. Fig. A1 shows these paths and the corresponding total stored energy density at 0.5% strain, which clearly demonstrate that the latter is indeed less than that observed at the boundary of the GOI at 51 μm depth. That is, the total stored energy density, which is argued here to locate the slip-assisted twin nucleation sites, is highest at the grain boundary compared to that of grain interior. This agrees well with the experimental evidence that the slip-assisted twin nucleation typically occurs at the grain boundaries.

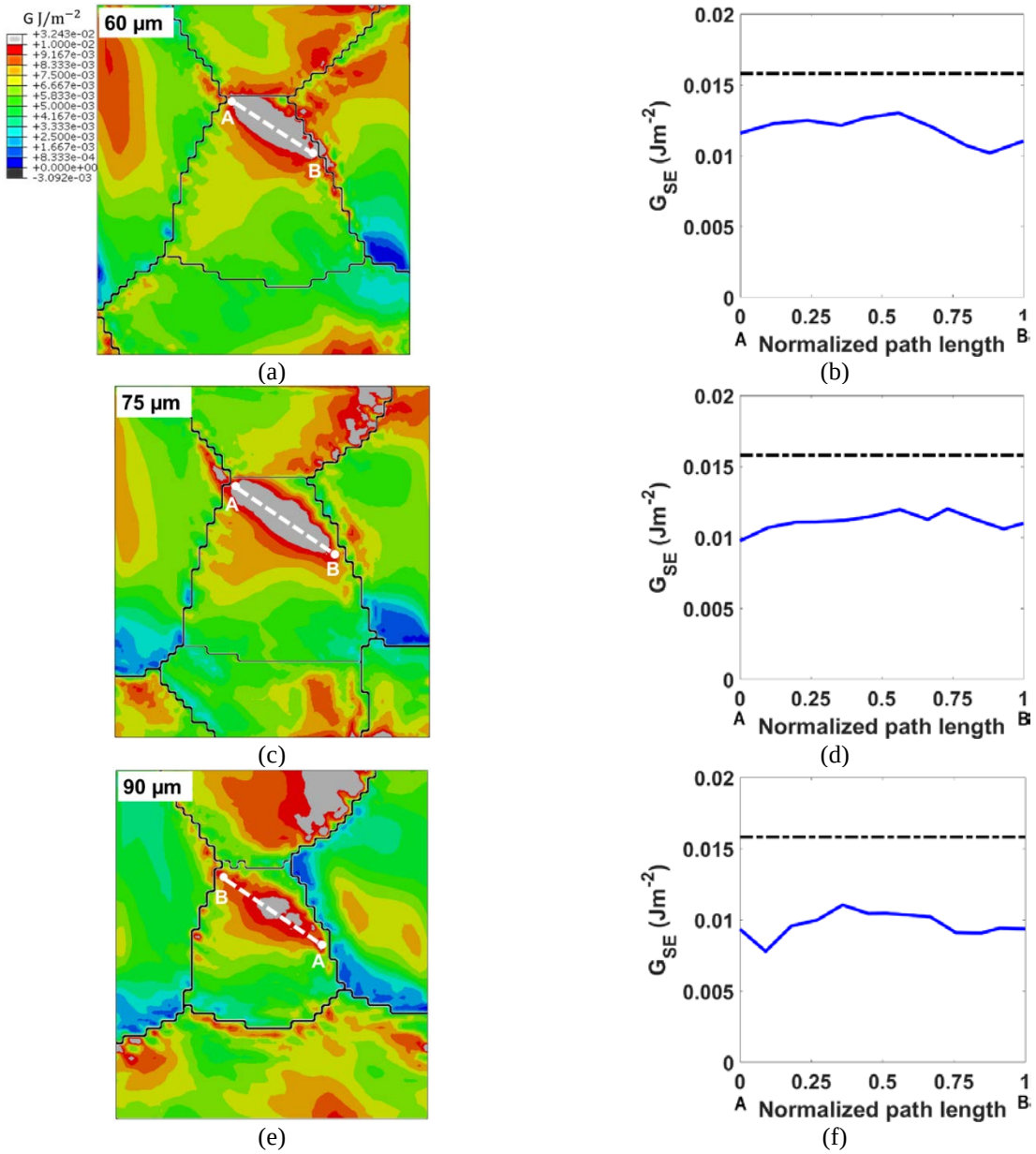

Figure A1 : The distribution, both spatial and along the defined paths (AB), of total stored energy density within the GOI at the depths of (a) and (b) 60 µm, (c) and (d) 75 µm, and (e) and (f) 90 µm. The dashed lines indicate the magnitude of total stored energy density (0.0158 Jm^{-2}) at 51 µm depth.

Appendix B. The distribution of total stored energy density within neighbouring grains

The numerical results in Table 5 show hotspots of the total stored energy density within neighbouring grains. In order to understand the magnitude of these distributions, the total stored energy density is measured along the perimeters and in the interiors of the neighbouring grains that possess high energy density. Table B1 shows these paths and corresponding total stored energy density. This quantification demonstrates that the energy density is less than that of the

critical value within majority of neighbouring grains except within grains P and Q at the depths of 15 μm and 30 μm respectively. These sections of the 3D microstructure are analysed in detail.

Table B1 : The sections of microstructure showing the spatial distribution of total stored energy density and that measured along the specified paths in the neighbours of the GOI

Stored energy density (FE model)	Total stored energy density measured along the specified path
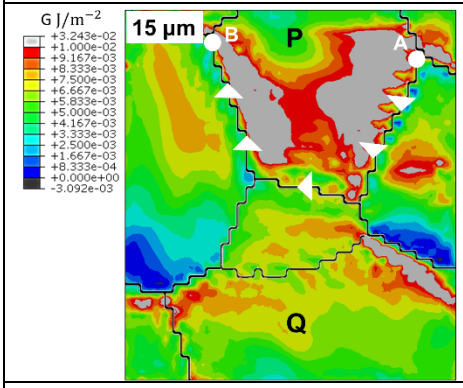	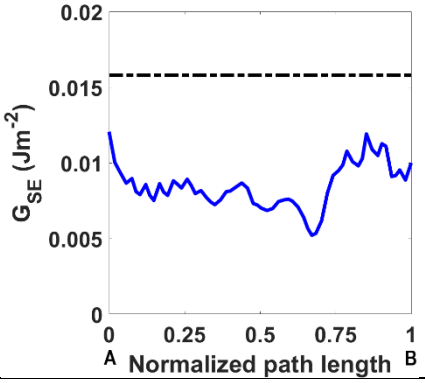
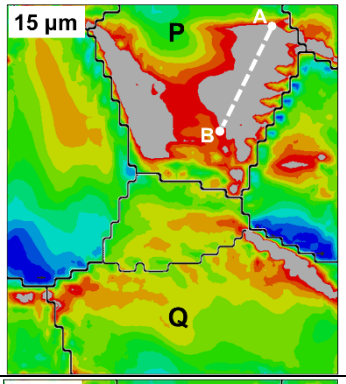	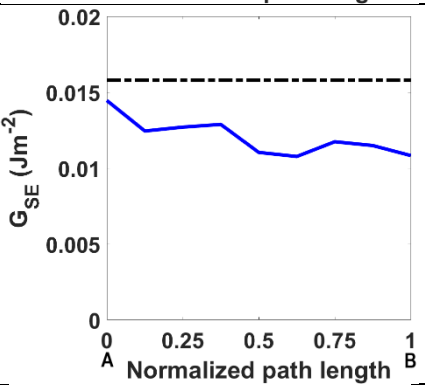
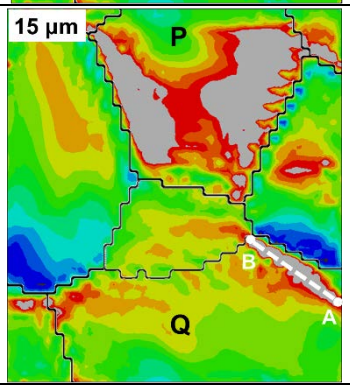	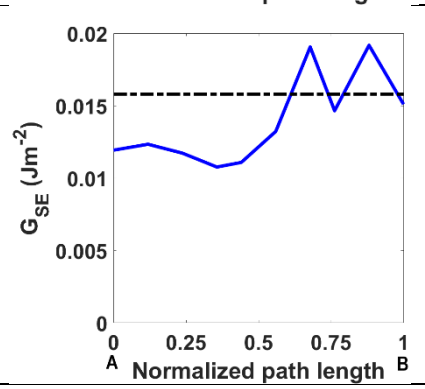

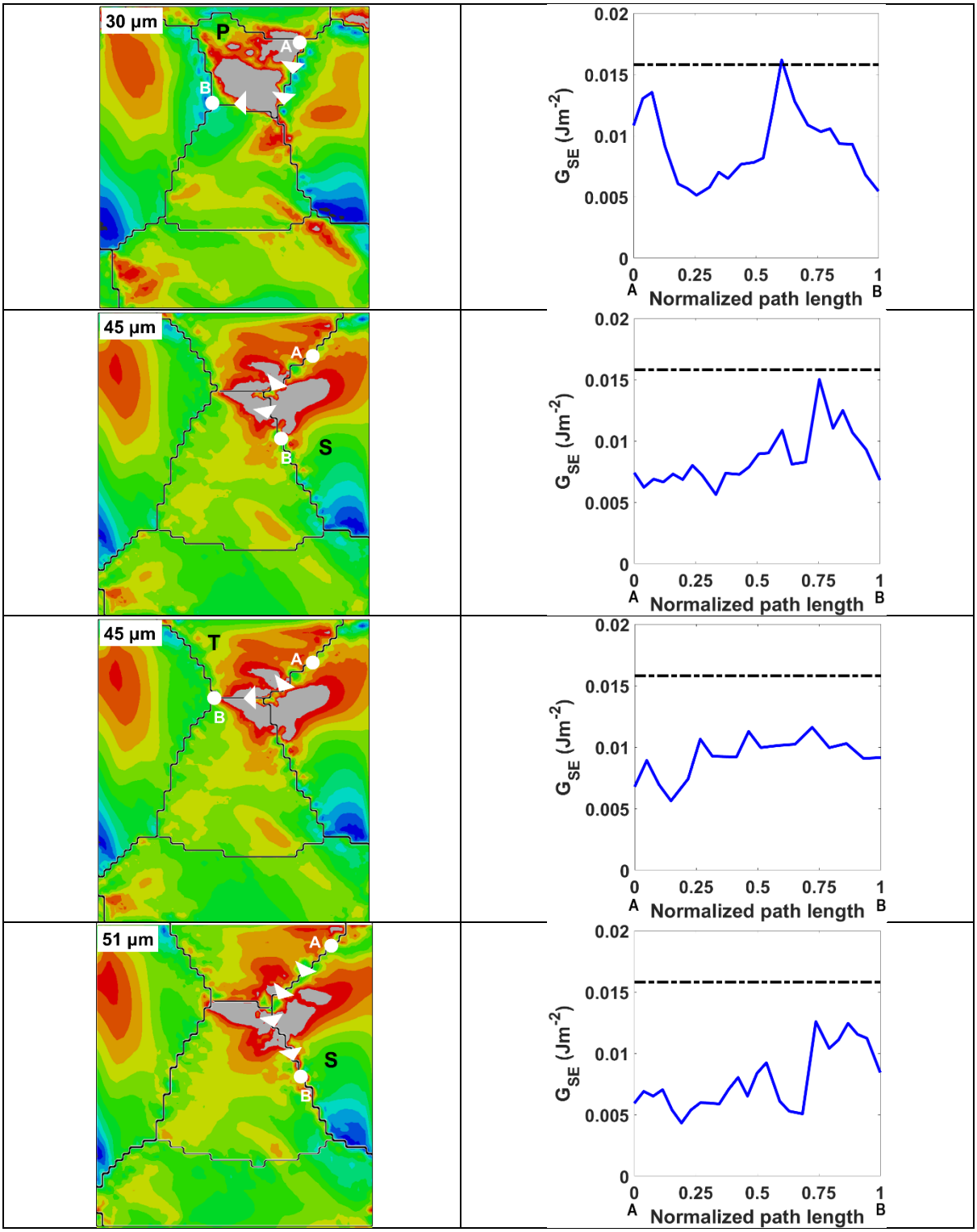
30 µm
P
A
B
45 µm
A
B
S
45 µm
T
A
B
51 µm
A
B
S
0.02
0.015
0.01
0.005
0
G_{SE} (Jm^{-2})
0
0.25
0.5
0.75
1
A
B
Normalized path length

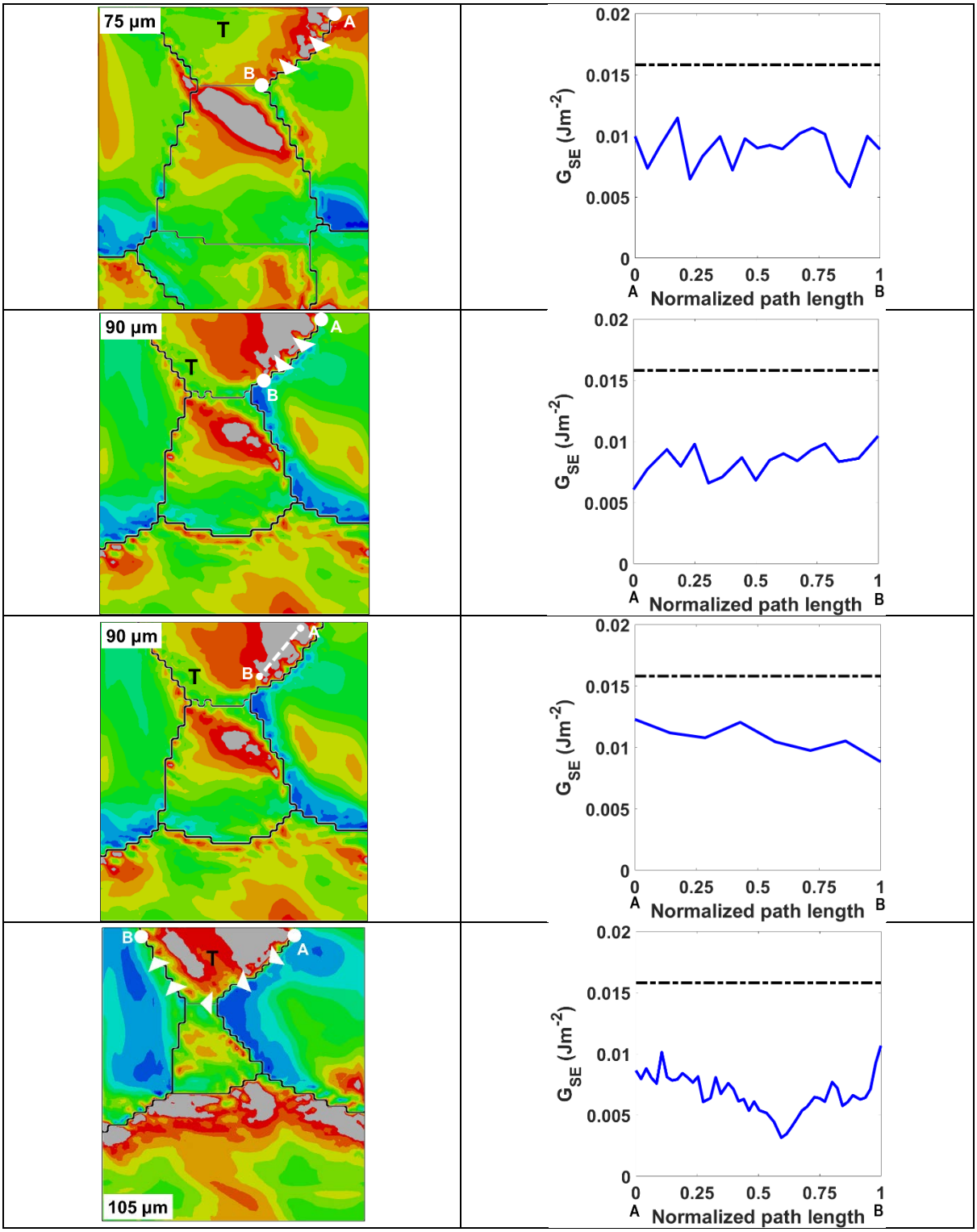
75 µm
T
A
B
90 µm
T
A
B
90 µm
T
A
B
B
T
A
105 µm
0.02
0.015
0.01
0.005
0
G_{SE} (Jm^{-2})
0
0.25
0.5
0.75
1
A
B
Normalized path length

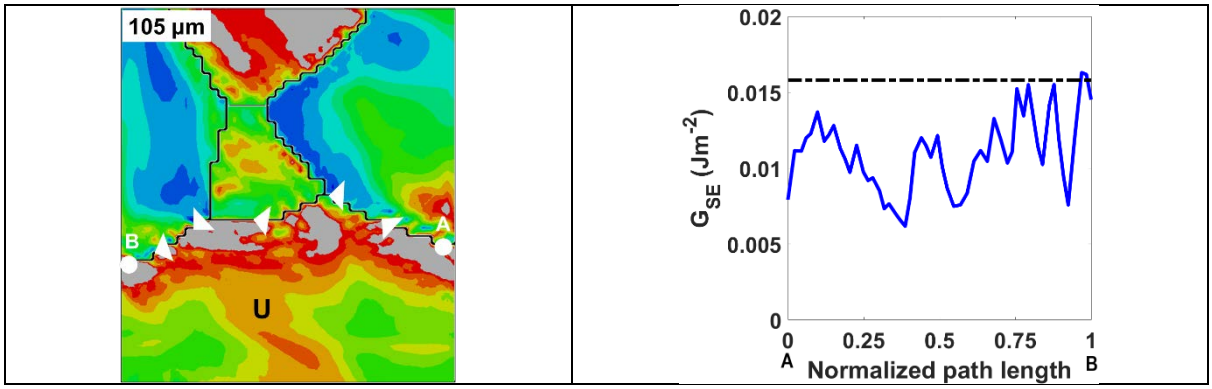

References

(Abdolvand and Daymond (2013)) Abdolvand, H., Daymond, M. R., 2013. Multi-scale modeling and experimental study of twin inception and propagation in hexagonal close-packed materials using a crystal plasticity finite element approach â€" part i: Average behavior. Journal of the Mechanics and Physics of Solids 61 (3), 783–802.

(Abdolvand et al. (2011)) Abdolvand, H., Daymond, M. R., Mareau, C., 2011. Incorporation of twinning into a crystal plasticity finite element model: evolution of lattice strains and texture in zircaloy-2. International Journal of Plasticity 27 (11), 1721–1738.

(Abdolvand et al. (2020)) Abdolvand, H., Louca, K., Mareau, C., Majkut, M., Wright, J., 2020. On the nucleation of deformation twins at the early stages of plasticity. Acta Materialia, doi.org/10.1016/j.actamat.2020.07.010.

(Al-Samman and Gottstein (2008)) Al-Samman, T., Gottstein, G., 2008. Room temperature formability of a magnesium az31 alloy: Examining the role of texture on the deformation mechanisms. Materials Science and Engineering: A 488 (1), 406–414.

(Ardeljan et al. (2017)) Ardeljan, M., Beyerlein, I. J., Knezevic, M., 2017. Effect of dislocation density-twin interactions on twin growth in az31 as revealed by explicit crystal plasticity finite element modeling. International Journal of Plasticity 99, 81–101.

(Arsenlis and Parks (1999)) Arsenlis, A., Parks, D., 1999. Crystallographic aspects of geometrically-necessary and statistically-stored dislocation density. Acta materialia 47 (5), 1597–1611.

(Barnett et al. (2014)) Barnett, M., Ghaderi, A., Da Fonseca, J. Q., Robson, J., 2014. Influence of orientation on twin nucleation and growth at low strains in a magnesium alloy. Acta Materialia 80, 380–391.

(Barnett et al. (2012)) Barnett, M. R., Nave, M. D., Ghaderi, A., 2012. Yield point elongation due to twinning in a magnesium alloy. Acta materialia 60 (4), 1433–1443.

(Barrett et al. (2012)) Barrett, C., El Kadiri, H., Tschopp, M., 2012. Breakdown of the schmid law in homogeneous and heterogeneous nucleation events of slip and twinning in magnesium. Journal of the Mechanics and Physics of Solids 60 (12), 2084–2099.

(Bell and Cahn (1953)) Bell, R., Cahn, R., 1953. The nucleation problem in deformation twinning. Acta Metallurgica 1 (6), 752–753.

(Beyerlein et al. (2010)) Beyerlein, I., Capolungo, L., Marshall, P., McCabe, R., Tomé, C., 2010. Statistical analyses of deformation twinning in magnesium. Philosophical Magazine 90 (16), 2161–2190.

(Beyerlein et al. (2011)) Beyerlein, I., McCabe, R., Tomé, C., 2011. Effect of microstructure on the nucleation of deformation twins in polycrystalline high-purity magnesium: A multi-scale modeling study. Journal of the Mechanics and Physics of Solids 59 (5), 988 – 1003.

(Beyerlein and Tomé (2010)) Beyerlein, I., Tomé, C., 2010. A probabilistic twin nucleation model for hcp polycrystalline metals. Proceedings of the Royal Society A: Mathematical, Physical and Engineering Sciences 466 (2121), 2517–2544.

(Burnett et al. (2016)) Burnett, T., Kelley, R., Winiarski, B., Contreras, L., Daly, M., Gholinia, A., Burke, M., Withers, P., 2016. Large volume serial section tomography by xe plasma fib dual beam microscopy. Ultramicroscopy 161, 119–129.

(Capolungo and Beyerlein (2008)) Capolungo, L., Beyerlein, I., 2008. Nucleation and stability of twins in hcp metals. Physical review B 78 (2), 024117.

(Capolungo et al. (2009)) Capolungo, L., Marshall, P., McCabe, R., Beyerlein, I., Tomé, C., 2009. Nucleation and growth of twins in zr: a statistical study. Acta Materialia 57 (20), 6047 – 6056.

(Cheng and Ghosh (2015)) Cheng, J., Ghosh, S., 2015. A crystal plasticity fe model for deformation with twin nucleation in magnesium alloys. International Journal of Plasticity 67, 148–170.

(Christian and Mahajan (1995)) Christian, J. W., Mahajan, S., 1995. Deformation twinning. Progress in materials science 39 (1-2), 1–157.

(Dunne et al. (2007)) Dunne, F., Rugg, D., Walker, A., 2007. Lengthscale-dependent, elastically anisotropic, physically-based hcp crystal plasticity: application to cold-dwell fatigue in ti alloys. International Journal of Plasticity 23 (6), 1061–1083.

(Easton et al. (2008)) Easton, M., Beer, A., Barnett, M., Davies, C., Dunlop, G., Durandet, Y., Blacket, S., Hilditch, T., Beggs, P., 2008. Magnesium alloy applications in automotive structures. Jom 60 (11), 57.

(Echlin et al. (2020)) Echlin, M. P., Burnett, T. L., Polonsky, A. T., Pollock, T. M., Withers, P. J., 2020. Serial sectioning in the sem for three dimensional materials science. Current Opinion in Solid State and Materials Science, 100817.

(Ghazisaeidi and Curtin (2013)) Ghazisaeidi, M., Curtin, W., 2013. Analysis of dissociation of< c> and< c+ a> dislocations to nucleate twins in mg. Modelling and Simulation in Materials Science and Engineering 21 (5), 055007.

(Godet et al. (2006)) Godet, S., Jiang, L., Luo, A., Jonas, J., 2006. Use of schmid factors to select extension twin variants in extruded magnesium alloy tubes. Scripta Materialia 55 (11), 1055–1058.

(Groeber and Jackson (2014)) Groeber, M. A., Jackson, M. A., 2014. Dream. 3d: a digital representation environment for the analysis of microstructure in 3d. Integrating Materials and Manufacturing Innovation 3 (1), 5.

(Guo et al. (2020)) Guo, Y., Collins, D. M., Tarleton, E., Hofmann, F., Wilkinson, A. J., Britton, T. B., 2020. Dislocation density distribution at slip band-grain boundary intersections. Acta Materialia 182, 172–183.

(Hazeli et al. (2015)) Hazeli, K., Askari, H., Cuadra, J., Streller, F., Carpick, R., Zbib, H., Kontsos, A., 2015. Microstructure-sensitive investigation of magnesium alloy fatigue. International Journal of Plasticity 68, 55–76.

(Heripre et al. (2007)) Heripre, E., Dexet, M., Crepin, J., Gélébart, L., Roos, A., Bornert, M., Caldemaison, D., 2007. Coupling between experimental measurements and polycrystal finite element calculations for micromechanical study of metallic materials. International Journal of Plasticity 23 (9), 1512–1539.

(Hill (1963)) Hill, R., 1963. Elastic properties of reinforced solids: some theoretical principles. Journal of the Mechanics and Physics of Solids 11 (5), 357–372.

(Jeong et al. (2018)) Jeong, J., Alfreider, M., Konetschnik, R., Kiener, D., Oh, S. H., 2018. In-situ tem observation of {101 2} twin-dominated deformation of mg pillars: Twinning mechanism, size effects and rate dependency. Acta Materialia 158, 407–421.

(Jonas et al. (2011)) Jonas, J. J., Mu, S., Al-Samman, T., Gottstein, G., Jiang, L., Martin, E., 2011. The role of strain accommodation during the variant selection of primary twins in magnesium. Acta Materialia 59 (5), 2046–2056.

(Khosravani et al. (2015)) Khosravani, A., Fullwood, D., Adams, B., Rampton, T., Miles, M., Mishra, R., 2015. Nucleation and propagation of twins in az31 magnesium alloy. Acta Materialia 100, 202–214.

(Kumar et al. (2017)) Kumar, M. A., Beyerlein, I. J., Tome, C. N., 2017. A measure of plastic anisotropy for hexagonal close packed metals: Application to alloying effects on the formability of mg. Journal of Alloys and Compounds 695, 1488–1497.

(Kumar et al. (2006)) Kumar, R., Wang, A.-J., McDowell, D., 2006. Effects of microstructure variability on intrinsic fatigue resistance of nickel-base superalloys–a computational micromechanics approach. International journal of fracture 137 (1-4), 173–210.

(Liu et al. (2018)) Liu, C., Shanthraj, P., Diehl, M., Roters, F., Dong, S., Dong, J., Ding, W., Raabe, D., 2018. An integrated crystal plasticity–phase field model for spatially resolved twin nucleation, propagation, and growth in hexagonal materials. International Journal of Plasticity 106, 203–227.

(Liu et al. (2017)) Liu, Y., Li, N., Kumar, M. A., Pathak, S., Wang, J., Mccabe, R. J., Mara, N. A., Tome, C. N., 2017. Experimentally quantifying critical stresses associated with basal slip and twinning in magnesium using micropillars. Acta Materialia 135, 411–421.

(Liu et al. (2019)) Liu, Y., Tang, P., Gong, M., McCabe, R., Wang, J., Tomé, C., 2019. Three-dimensional character of the deformation twin in magnesium. Nature communications 10 (1), 3308.

(McClelland et al. (2015)) McClelland, Z., Li, B., Horstemeyer, S., Brauer, S., Adedoyin, A., Hector Jr, L., Horstemeyer, M., 2015. Geometrically necessary twins in bending of a magnesium alloy. Materials Science and Engineering: A 645, 298–305.

(Mendelson (1969)) Mendelson, S., 1969. Zonal dislocations and twin lamellae in hcp metals. Materials Science and Engineering 4 (4), 231–242.

(Molodov et al. (2016)) Molodov, K. D., Al-Samman, T., Molodov, D. A., Gottstein, G., 2016. On the role of anomalous twinning in the plasticity of magnesium. Acta Materialia 103, 711–723.

(Nye (1953)) Nye, J., 1953. Some geometrical relations in dislocated crystals. Acta metallurgica 1 (2), 153–162.

(Paramatmuni and Dunne (2020)) Paramatmuni, C., Dunne, F. P., 2020. Effect of twin crystallographic orientation on deformation and growth in mg alloy az31. International Journal Plasticity, doi.org/10.1016/j.ijplas.2020.102775.

(Paramatmuni and Kanjarla (2019)) Paramatmuni, C., Kanjarla, A. K., 2019. A crystal plasticity fft based study of deformation twinning, anisotropy and micromechanics in hcp materials: Application to az31 alloy. International Journal of Plasticity 113, 269 – 290.

(Paramatmuni et al. (2020)) Paramatmuni, C., Zheng, Z., Rainforth, W. M., Dunne, F. P., 2020. Twin nucleation and variant selection in mg alloys: An integrated crystal plasticity modelling and experimental approach. International Journal of Plasticity 135, 102778.

(Prasad et al. (2014)) Prasad, K. E., Rajesh, K., Ramamurty, U., 2014. Micropillar and macropillar compression responses of magnesium single crystals oriented for single slip or extension twinning. Acta materialia 65, 316–325.

(Price (1961)) Price, P., 1961. Nucleation and growth of twins in dislocation-free zinc crystals. Proceedings of the Royal Society of London. Series A. Mathematical and Physical Sciences 260 (1301), 251–262.

(Qiao et al. (2016)) Qiao, H., Barnett, M., Wu, P., 2016. Modeling of twin formation, propagation and growth in a mg single crystal based on crystal plasticity finite element method. International Journal of Plasticity 86, 70–92.

(Robson and Barnett (2019)) Robson, J. D., Barnett, M. R., 2019. The effect of precipitates on twinning in magnesium alloys. Advanced Engineering Materials 21 (4), 1800460.

(Robson et al. (2010)) Robson, J. D., Stanford, N., Barnett, M. R., 2010. Effect of particles in promoting twin nucleation in a mg–5 wt.% zn alloy. Scripta materialia 63 (8), 823–826.

(Stanford et al. (2012)) Stanford, N., Taylor, A. S., Cizek, P., Siska, F., Ramajayam, M., Barnett, M. R., 2012. {101 2} twinning in magnesium-based lamellar microstructures. Scripta Materialia 67 (7-8), 704–707.

(Terada et al. (2000)) Terada, K., Hori, M., Kyoya, T., Kikuchi, N., 2000. Simulation of the multi-scale convergence in computational homogenization approaches. International Journal of Solids and Structures 37 (16), 2285–2311.

(Tomé et al. (1991)) Tomé, C., Lebensohn, R. A., Kocks, U., 1991. A model for texture development dominated by deformation twinning: application to zirconium alloys. Acta metallurgica et materialia 39 (11), 2667–2680.

(Tromans (2011)) Tromans, D., 2011. Elastic anisotropy of hcp metal crystals and polycrystals. Int. J. Res. Rev. Appl. Sci 6 (4), 462–483.

(Van der Sluis et al. (2000)) Van der Sluis, O., Schreurs, P., Brekelmans, W., Meijer, H., 2000. Overall behaviour of heterogeneous elastoviscoplastic materials: effect of microstructural modelling. Mechanics of Materials 32 (8), 449–462.

(Wang et al. (2010a)) Wang, J., Beyerlein, I., Tomé, C., 2010. An atomic and probabilistic perspective on twin nucleation in mg. Scripta Materialia 63 (7), 741–746.

(Wang et al. (2014)) Wang, J., Beyerlein, I., Tomé, C., 2014. Reactions of lattice dislocations with grain boundaries in mg: implications on the micro scale from atomic-scale calculations. International Journal of Plasticity 56, 156–172.

(Wang et al. (2009a)) Wang, J., Hirth, J., Tomé, C., 2009. (1 012) twinning nucleation mechanisms in hexagonal-close-packed crystals. Acta Materialia 57 (18), 5521–5530.

(Wang et al. (2009b)) Wang, J., Hoagland, R., Hirth, J., Capolungo, L., Beyerlein, I., Tomé, C., 2009. Nucleation of a twin in hexagonal close-packed crystals. Scripta Materialia 61 (9), 903–906.

(Wang et al. (2019)) Wang, J., Ramajayam, M., Charrault, E., Stanford, N., 2019. Quantification of precipitate hardening of twin nucleation and growth in mg and mg-5zn using micro-pillar compression. Acta Materialia 163, 68–77.

(Wang and Stanford (2015)) Wang, J., Stanford, N., 2015. Investigation of precipitate hardening of slip and twinning in mg5% zn by micropillar compression. Acta Materialia 100, 53–63.

(Wang et al. (2013)) Wang, J., Yadav, S., Hirth, J., Tomé, C., Beyerlein, I., 2013. Pure-shuffle nucleation of deformation twins in hexagonal-close-packed metals. Materials Research Letters 1 (3), 126–132.

(Wang et al. (2010b)) Wang, L., Eisenlohr, P., Yang, Y., Bieler, T., Crimp, M., 2010. Nucleation of paired twins at grain boundaries in titanium. Scripta Materialia 63 (8), 827–830.

(Wang et al. (2020)) Wang, X., Mao, P., Liu, Z., Wang, Z., Wang, F., Zhou, L., Wei, Z., 2020. Nucleation and growth analysis of {101â€¾ 2} extension twins in az31 magnesium alloy during in-situ tension. Journal of Alloys and Compounds 817, 152967.

(Wu et al. (2015)) Wu, P., Guo, X., Qiao, H., Lloyd, D., 2015. A constitutive model of twin nucleation, propagation and growth in magnesium crystals. Materials Science and Engineering: A 625, 140–145.

(Xu et al. (2021)) Xu, Y., Wan, W., Dunne, F. P., 2021. Microstructural fracture mechanics: Stored energy density at fatigue cracks. Journal of the Mechanics and Physics of Solids 146, 104209.

(Yang et al. (2008)) Yang, F., Yin, S., Li, S., Zhang, Z., 2008. Crack initiation mechanism of extruded az31 magnesium alloy in the very high cycle fatigue regime. Materials Science and Engineering: A 491 (1-2), 131–136.

(Yue and Weinan (2007)) Yue, X., Weinan, E., 2007. The local microscale problem in the multiscale modeling of strongly heterogeneous media: Effects of boundary conditions and cell size. Journal of Computational Physics 222 (2), 556–572.

(Zhang et al. (2015)) Zhang, C., Li, H., Eisenlohr, P., Liu, W., Boehlert, C., Crimp, M., Bieler, T., 2015. Effect of realistic 3d microstructure in crystal plasticity finite element analysis of polycrystalline ti-5al-2.5 sn. International Journal of Plasticity 69, 21–35.

(Zhang et al. (2007)) Zhang, M., Zhang, J., McDowell, D., 2007. Microstructure-based crystal plasticity modeling of cyclic deformation of ti–6al–4v. International Journal of Plasticity 23 (8), 1328–1348.

(Zheng et al. (2019)) Zheng, Z., Prastiti, N. G., Balint, D. S., Dunne, F. P., 2019. The dislocation configurational energy density in discrete dislocation plasticity. Journal of the Mechanics and Physics of Solids 129, 39–60.